



Provided by the author(s) and University of Galway in accordance with publisher policies. Please cite the published version when available.

Title	A process-structure-property model for welding of 9Cr power plant components: The influence of welding process temperatures on in-service cyclic plasticity response
Author(s)	Mac Ardghail, Padraig; Harrison, Noel M.; Leen, Sean B.
Publication Date	2019-04-30
Publication Information	Mac Ardghail, P., Harrison, N., & Leen, S. B. (2019). A process-structure-property model for welding of 9Cr power plant components: The influence of welding process temperatures on in-service cyclic plasticity response. <i>International Journal of Pressure Vessels and Piping</i> , 173, 26-44. doi: https://doi.org/10.1016/j.ijpvp.2019.04.015
Publisher	Elsevier
Link to publisher's version	https://doi.org/10.1016/j.ijpvp.2019.04.015
Item record	http://hdl.handle.net/10379/15585
DOI	http://dx.doi.org/10.1016/j.ijpvp.2019.04.015

Downloaded 2024-04-26T11:24:20Z

Some rights reserved. For more information, please see the item record link above.



A process-structure-property model for welding of 9Cr power plant components: the influence of welding process temperatures on in-service cyclic plasticity response

P. Mac Ardghail^{1,2}, N. Harrison^{1,2,3}, S.B. Leen^{1,2,3}

¹ Mechanical Engineering, College of Engineering and Informatics, National University of Ireland Galway, Galway, Ireland.

² Ryan Institute for Environmental, Marine and Energy Research, National University of Ireland Galway, Galway, Ireland

³ I-Form Advanced Manufacturing Research Centre, Ireland

Abstract

A process-structure-property methodology is presented for welding of 9Cr steels under representative flexible operating conditions for a typical thermal power plant girth-welded pipe. The welding-induced evolution of microstructural variables is represented via (i) a solid-state phase transformation model for martensite-austenite transformation and (ii) empirical equations for prior austenite grain size, martensite lath width, hardness and $M_{23}C_6$ precipitate diameter and area fraction, calibrated from published heat treatment data. The temperature-dependent, physically-based, unified viscoplastic constitutive model, which includes a fatigue damage initiation criterion, is based on dislocation density evolution and is validated against high temperature cyclic plasticity data at a range of relevant temperatures for parent material P91, including combined isotropic-kinematic hardening effects. This model is shown to successfully predict weld-life reduction factor for cross-weld tests. The effects of key welding process variables on the microstructure gradient in the heat-affected zone, and associated thermo-mechanical, cyclic plasticity response are assessed. The inter-critical and fine-grained heat-affected zones are identified as the critical regions, consistent with observed plant experience. Increasing post-weld heat-treatment temperature from 760°C from 780 °C is predicted to be detrimental due to increased precipitate coarsening. In contrast, increasing preheat and interpass temperature from 350°C to 400°C is predicted to be beneficial due to increased hardness in the critical regions.

1. Introduction

Welded connections represent key locations for failure in thermal power plant. The present work is focussed on the development of a process-structure-property methodology for predicting the effect of welding process on microstructure of weld-affected regions in power plant welds and hence, on the mechanical response. Such plant has traditionally operated under ‘base-load’ conditions, where power output was steady and near-constant throughout the life of the power plant. Creep was the dominant mode of deformation and creep failure the dominant failure mechanism; hence, the relevant steels were formulated to resist creep [1]. Among those creep-resistant steels are the 9Cr family of steels. These steels owe their strength to high-dislocation-density martensitic microstructures with nano-precipitate strengthening [2]. However, modern plant operating conditions are increasingly required to operate under flexible operating conditions to facilitate increased reliance on renewable energy sources and due to improved monitoring of the power grid, which permits more efficient operation by adjusting plant output to suit demand. Such operation leads to increased cyclic variations in steam pressure and temperature, thereby subjecting material to cyclic loading whether by high-temperature, low-cycle fatigue, creep-fatigue or thermomechanical fatigue (HTLCF, CF, TMF, respectively). The 9Cr microstructure degrades under cyclic conditions [3] and the steel softens, leading to a reduced service life. The worst-affected region tends to be heat-affected zone (HAZ), adjacent to the parent material (PM), and especially the inter-critical heat-affected zone (ICHAZ) of welded joints [4-6].

This work is focussed on the development of a weld-design tool for industry, so that plant designers and operators can specify welding processes which maximise the service life of plant components. The creep behaviour of welded P91 has received significant attention, including the development of small-scale test methods [7-9] for characterisation of heat-affected zone creep behaviour and the development of damage mechanics methods for creep assessment of welded test specimens and power plant components [10-14]. Some authors have also studied the high temperature fatigue and creep-fatigue of welded P91 test specimens. Farragher et al. [5] presented characterisation of the high temperature low cycle fatigue response of cross-weld P91 test specimens,

allowing inverse estimation of cyclic plasticity parameters (e.g. for isotropic-kinematic hardening) of an assumed homogeneous HAZ region. A two-layer visco-plasticity material model was used for the welded connections, allowing cyclic viscoplasticity with combined (non-linear) kinematic-isotropic hardening-softening, and a Norton-type equation for strain-rate effects. More recently, Touboul et al. [15] presented a method for identification of the viscoplastic properties of three different HAZ regions for P91, viz. ICHAZ, fine-grain HAZ and coarse-grain HAZ, at elevated temperature (625°C) using digital imaging correlation (DIC) on a cross-weld (CW) specimen. Fournier et al. [16] proposed a physically-based model for the high temperature cyclic behaviour of 9Cr steel. . Other authors have also proposed unified viscoplasticity models for 9Cr steel. For example, Kyaw et al. [17] developed a unified viscoplasticity model for parent metal P91 that included kinematic hardening, cyclic softening and coupled damage. Benaarbia et al. [18] proposed a model that predicted the response of P91 under cyclic conditions as well as under cyclic conditions with stress-relaxation dwells. These two models agreed well with experimental test results but they were not applied to welded components. Numerous creep models, some examples of which are reviewed by Rouse et al. [19], have been applied to 9Cr steel, e.g. [20, 21], including physically-based creep models applied to CW specimens [22].

However, the present work adopts a fundamentally different approach to the previously published work, by starting with the welding process itself and predicting the effect of the welding process on the microstructure and hence on the high temperature constitutive response of the welded joint. A key benefit of this approach is that it circumvents the need to idealise the heat-affected region into a discrete number of zones, e.g. two- [23], three- [14, 24], four- [25] or five-material [13, 26] models, and more importantly, the need to measure the behaviour of such zones, which is inherently difficult due to the small sizes of such zones. In the present approach, the naturally-occurring gradient in microstructure is represented. The authors have already presented the basis for this work [27] with application to uniaxial cross-weld test specimens.

Much of the aforementioned work pertained to modelling 9Cr steel PM or CW specimens. Attempts to model entire 9Cr power plant components have included modelling of welding-induced residual stress [28, 29] in pipe sections, as a guide to select appropriate PWHT conditions, but in-service operation was not considered. Rouse et al. [30] used

neural networks to predict thermal stresses in power plant components but all weld regions used the same material properties. Li et al. [24] looked at a welded power plant tee-joint, treating the weld as an idealised three-material region, comprising of HAZ, WM and PM.

A key novelty of this work is the coupling of thermal history, microstructure evolution and mechanical behaviour in a process-structure-property framework for a representative pipe geometry. This allows for microstructure-prediction in welding and PWHT of P91 and prediction of the welded pipe response under cyclic thermomechanical loading conditions, based on the through-process predicted microstructure across welded zones.

A previous paper by the authors [27] focused on the HTLCF performance of welded P91 specimens and demonstrated the capability of the present approach to predict weld life reduction. This paper presents a further development of the latter, as follows:

- Introducing additional complexities to the microstructure variables considered, specifically including the key effects of carbide precipitates, via inclusion of a precipitate evolution model. Precipitates are a key strengthening mechanism of 9Cr steel due to their dislocation-pinning effects and their long-term evolution, e.g. during in-service operation, allowed for microstructure influences on performance to be included beyond those caused only by welding and PWHT. An example of this is the inclusion of a precipitate-based yield stress.
- **Calibrating the current model against a larger set of cyclic test data.**
- **Reducing the number of model parameters to be identified.**
- **Extension of through-process methodology to include the weld metal.**
- Applying the model to the significantly more complex case of a real pipe girth weld (compared to a cross weld tensile specimen), under a steam pressure-temperature history representative of flexible operation, with a view to elucidating the effects on flexible operating response.
- Examining the effects of key welding process variables on the cyclic response of the welding-affected material zones, including the welding-induced continuous gradient in microstructure and hence properties. This demonstrates the design-tool capability of the through-process methodology for identification of optimal welding parameters.

- Including the effects of welding-induced residual stresses on microstructure-sensitive cyclic response.

2. Methodology

2.1 General

The fundamental process-structure-property methodology adopted here is similar to that previously presented [27]. In that paper, the methodology was applied to successfully predict the weld-life reduction factor (WLRF) for uniaxial HTLCF testing of P91 cross-weld specimens. The first part of the methodology is a thermal model of the multi-pass welding process, for predicting the distribution of temperature-time histories, implemented in the general-purpose finite element software Abaqus. The temperature histories were used as input to the second part of the through-process methodology (microstructure evolution), to predict evolution of phases (tempered and untempered martensite and austenite) and of hardness, lath width and prior austenite grain size (PAG), and, in the case of including residual stress effects, a sequential thermo-mechanical simulation of the welding process. The essential aspects of this are summarised here for completeness. In the present work, we now add evolutions of carbide precipitate diameter and area fraction evolution. The third part of the methodology is the thermo-mechanical simulation of the in-service time-varying pressure-temperature history, representative of flexible operating conditions. This uses a microstructure-dependent thermo-mechanical, unified viscoplasticity constitutive model to predict the temperature-dependent cyclic plasticity response of the welded joint. Of particular interest is (i) the predicted evolution of cross-weld, inhomogeneous stress distributions, due to the welding-induced gradients in microstructure, and (ii) the predicted evolution of the microstructure variables, such as carbide precipitates. The microstructure-evolution and constitutive models were implemented in the finite element software package Abaqus using a custom-developed user-material subroutine (UMAT), which allowed the full through-process model to be applied to a single FE geometry.

The microstructure model includes the following aspects: austenite and martensite phases, prior-austenite grain (PAG) size, hardness, lath width and $M_{23}C_6$ precipitate diameter and area fraction.

2.2 Thermal model for multi-pass welding process

A transient thermal model for multi-pass gas tungsten arc welding (GTAW) of an axisymmetric pipe was developed, following the methodology of Yaghi et al. [29] and similar to the approach previously presented by Mac Ardghail et al. [27] for a HTLCF cross-weld specimen. An element-birth method is used to activate mesh regions corresponding to individual weld beads. Figure 1 shows sample temperature contour distributions for the 24-pass model, for different numbers of completed passes.

For the welding simulation, preheat and inter-pass temperature was either 350°C or 400°C (see Table 1). The entire geometry (Fig. 2) was heated to this temperature before the first weld bead was laid and throughout the welding simulation, the sink temperature for the convection heat transfer was 350°C or 400°C, ensuring that the material would not cool below the inter-pass temperature.

For the weld beads, the temperature load was applied as a temperature boundary condition with a 1 second ramp from 350°C or 400°C to a peak temperature, which was selected to ensure that each weld bead surpassed the material melt temperature of 1500°C, followed by a 0.5s hold at peak temperature. The welding simulation contained 24 weld passes, as shown in Fig. 2. The temperature boundary condition used in this work is representative of gas tungsten arc welding (GTAW) with a voltage of 28 volts, a current of 200 amps and a torch speed of 4.66 mm/s. It served as a means of locally heating the material to representative temperatures with representative heating and cooling rates to ensure representative microstructure evolution.

The pipe model is axisymmetric, with a wall thickness was 36 mm. The internal diameter for the pipe is 300 mm and the length of the modelled pipe section is 300 mm. The chamfer-angle for the weld metal is 60° and the two ends of the pipe are 4 mm apart prior to welding. For the heat-transfer analysis, 8-node quadrilateral elements are used and for mechanical simulations, 8-node reduced-integration biquadratic quadrilateral elements are used.

2.3 Solid state phase transformation model

The special-purpose Abaqus user-material (UMAT) subroutine, developed in [27] is adopted here to compute solid-state phase evolution, based on temperature history and the phase equilibrium diagram. The solid-state phases considered are austenite (γ) and martensite (α'). Volume-fraction evolution for austenite, V_γ , is defined with a linear lever rule:

$$V_\gamma = 1 - \frac{A_{c3} - T}{A_{c3} - A_{c1}} \quad (1)$$

where A_{c3} (924°C) is the finish temperature for austenite transformation, A_{c1} (830°C) is the start temperature for austenite transformation and T is the current temperature. The values of A_{c1} and A_{c3} were obtained from Yaghi et al. [31]. **The linear lever rule is considered appropriate due to the rapidity of the austenite transformation expected during welding processes, similar to Hamelin et al. [32], who used a lever rule for rapid martensitic transformation.** For martensitic transformation, the Koistinen-Marburger function [33], was used as follows:

$$V_{\alpha'} = \lambda(1 - \exp[-0.011(M_s - T)]) \quad (2)$$

where M_s (400°C) is the martensite transformation start temperature according to the continuous cooling transformation (CCT) diagram, from the steel manufacturer Vallourec [34], and T is current temperature. λ is a constant used to ensure that martensite volume fraction reaches a value of 1 by the time the material reaches 100°C, the martensitic transformation finish temperature, M_f . In this work, it is assumed that only austenite exists at high temperatures (e.g. above A_{c3}) and only martensite exists at low temperatures (e.g. below M_f during quenching and below A_{c1} during in-service operation), as implied by the CCT diagram and by the phase equilibrium diagram from Cerjak et al. [35] for 9Cr steels. For simplicity, and due to the high delta-ferrite start temperature of around 1200°C [35], the present work does not simulate the formation of delta-ferrite. The solidus and liquidus temperatures are obtained from the literature [29] and are taken as 1450°C and 1500°C, respectively. A sample result for the temperature-phase evolution is shown in Fig. 3.

Metallurgical strain is attributed to volume increase caused by (a) austenitic transformation counteracting heating-induced expansion, and (b) martensitic transformation counteracting cooling-induced contraction, as described by Francis et al. [36]. This is modelled here via the following equations [28, 31]:

$$\Delta\varepsilon_{MET-\gamma} = \lambda_2 \frac{\Delta T}{A_{c3} - A_{c1}} \quad (3)$$

$$\Delta\varepsilon_{MET-\alpha'} = \lambda_3 \Delta T \exp[-0.011(M_s - T)] \quad (4)$$

where λ_2 and λ_3 are constants and ΔT is the incremental change in temperature. λ_2 is taken to be 0.244% [31] and λ_3 is taken to be 0.75% [28]. The parameters for the phase transformation model are shown in Table 2.

2.4 Prior austenite grain (PAG) evolution model

The evolution of PAGs is a modification of the approach presented by Mac Ardghail et al [27], but uses fewer parameters, more easily identifiable from heat treatment data. It is defined in two parts, corresponding to recrystallization and grain growth. The first part is given in incremental form as:

$$d(t + \Delta t) = (d(t) - d_{\min})(1 - \Delta S) + d_{\min} \quad (5)$$

where $d(t + \Delta t)$ is the updated grain size and $d(t)$ is the current grain size. d_{\min} is minimum grain size, with recrystallized volume fraction, S , defined to evolve as follows:

$$\Delta S = c_1 \Delta T \quad \text{For } \dot{T} > 0 \quad (6)$$

where c_1 is a constant and $\dot{T} = \Delta T / \Delta t$, where t is time. In this work, a dot over a variable indicates differentiation with respect to time. The recrystallized volume fraction is initially zero. When recrystallisation completes ($S = 1$), grain growth may occur:

$$\dot{d} = \frac{c_2}{d} \quad (7)$$

where

$$c_2 = c_3 e^{c_4 T} \quad (8)$$

with c_3 and c_4 as constants. This model was calibrated against simulated welding data from Milovic et al. [37], as shown in Fig. 4. The parameters for the grain evolution model are shown in Table 2.

2.5 Vickers hardness and lath width evolution model

The hardness evolution model is also improved relative to that presented previously, again by reduction in the number of parameters. The hardness H , is assumed to follow the following equation:

$$\dot{H} = \mu_1(H_L - H) \quad (9)$$

where

$$\mu_1 = \mu_2 + \mu_3 T \quad (10)$$

and

$$H_L = \mu_4 + \mu_5 T \quad (11)$$

with μ_2 to μ_5 as constants. During tempering, the softening is found to be well represented by an asymptotic equation; this equation can also be adopted for hardening during welding and is reflective of the physical processes controlling hardness, such as the formation of high dislocation-density, newly-formed martensite. This is partially controlled by the carbon content of the steel. The material cannot get infinitely harder so a limiting value is assumed. The hardness model was calibrated against data from Potirniche et al. [38], as shown in Fig. 5, leading to the identified parameters shown in Table 3.

The lath width, L , evolution model used here is also improved relative to that used previously [27] It is more physically realistic by virtue of the lath width being independent of PAG size, as follows:

$$\dot{L} = \mu_6(L_{\text{Lim}} - L) + \mu_7 \dot{H} \quad (12)$$

where

$$L_{\text{Lim}} = \mu_8 e^{\mu_9 T} \quad (13)$$

is an asymptotic limit for the lath width during short-term heat treatment with μ_6 to μ_9 as constants. As shown in Figure 6a, the first term in Eqn. 12 was calibrated against data from Ennis et al. [2] for relatively short time durations whereas the second term, which allows for lath evolution over longer time durations, was calibrated against data from Barbadikar et al. [39], as shown in Fig. 6b. The latter is important for through-process modelling and prediction of in-service behaviour. The identified parameters are shown in Table 3.

2.5 $M_{23}C_6$ precipitate evolution model

Precipitate modelling is a new feature relative to the previous work published by the authors [27]. Carbide precipitates are a key strengthening mechanism in 9Cr steel because they help to pin dislocations. However, carbides can coarsen during in-service loading, and thus may have significant influence on component behaviour, e.g. as carbides coarsen or

are consumed by Laves phase, the material weakens. In this work, the $M_{23}C_6$ precipitate area fraction and diameter is modelled.

The area fraction of precipitates, A_θ , is defined to evolve as follows during PWHT:

$$\dot{A}_\theta = \frac{m_1}{m_2 + A_\theta} \quad (14)$$

where

$$m_1 = m_3 + m_4 T \quad (15)$$

with m_2 , m_3 and m_4 as constants. Equation 14 is of a similar form to Eqn. 7. If the area-fraction of $M_{23}C_6$ precipitates increases then carbon is removed from the surrounding martensite matrix. Equations 14 and 15 were calibrated against P92 data [39], taken here as representative of P91, in the absence of published data for the latter, as shown in Fig. 7.

When the material reaches high temperatures during welding, the area fraction of precipitates reduces, due to precipitates going into solution. Phase calculations by Shen et al. [40] showed a rapid decrease in the mole % phase of $M_{23}C_6$ above a temperature of about 800°C. It is assumed that the area fraction of precipitates follows a similar reduction. A linear relationship with temperature was assumed since the dissolution process appears to be rapid:

$$\dot{A}_\theta = n_1 T \quad (16)$$

where n_1 is a constant.

The precipitate diameter, θ , evolution during PWHT, creep and ageing is defined as follows:

$$\dot{\theta} = \left(\frac{m_5}{m_6 + \theta} \right) \left(1 - \frac{\theta}{\theta_L} \right)^{m_7} \quad (17)$$

where

$$\theta_L = m_8 + m_9 T + m_{10} \sigma \quad (18)$$

is a limiting value and m_5 to m_{10} are constants. Equations 17 and 18 were calibrated against published representative data from a range of sources [2, 39, 41-43], as shown in Fig. 7.

Note that Fig. 7b shows the results of calibration against short-term heat treatment (tempering) data above 700°C while Fig. 7c shows calibration results for long-term heat treatment (ageing) below 700°C. Similar to the reduction in the area fraction of precipitates in Eqn. 14, the precipitate diameter decreases at high temperatures:

$$\dot{\theta} = n_2 T \quad (19)$$

where n_2 is a constant. The model parameters for Eqns. 14 to 19 are shown in Table 4.

2.6 Physically-based, unified viscoplasticity constitutive model

The physically-based, constitutive model implemented here is a modified version of that presented by Mac Ardghail et al [27]. One key difference is the incorporation of a precipitate size dependent yield stress, to account for the effects of precipitate coarsening, particularly during in-service conditions. It is based on dislocation mechanics theory and incorporates both isotropic softening and kinematic hardening, using Taylor type formulations in both cases. Key inputs to this model include the results from the microstructure-evolution model, specifically, the volume-fractions of solid-state phases (tempered and newly-formed martensite, austenite), PAG size, lath-width and $M_{23}C_6$ precipitate diameter and area-fraction, as described below. The model was implemented here within an Abaqus UMAT.

The rate of equivalent plastic strain \dot{p} is described using a hyperbolic sine flow rule as follows:

$$\dot{p} = \alpha \sinh(\beta f) \quad (20)$$

where α and β are identified from monotonic data for P92 following the method described elsewhere [27]. In this work, the number of constitutive parameters has also been reduced. It has been possible to identify a constant value for β while α is defined as proportional to the PAG size:

$$\alpha = n_3 d \quad (21)$$

where n_3 is a constant. As d increases, so does the visco-plastic strain-rate (Eqn. 20), consistent with previously published work [44]. The parameters for the hyperbolic sine flow rule are displayed in Table 3. The yield function f is defined as:

$$f = \sqrt{\frac{3}{2}(\boldsymbol{\sigma}' - \boldsymbol{\chi}') : (\boldsymbol{\sigma}' - \boldsymbol{\chi}') + R - k} \quad (22)$$

where $\boldsymbol{\sigma}'$ is the deviatoric stress tensor, $\boldsymbol{\chi}'$ is the deviatoric kinematic back-stress tensor, and $:$ represents the scalar product of two tensors. R is an isotropic softening variable, representing the change (decrease) in size of the yield surface.

The room-temperature yield stress for martensite (tempered or untempered), σ_y^0 , is defined to be a function of the precipitate-diameter and precipitate area-fraction, based on data from Barbadikar et al. [39]:

$$\sigma_y^0 = q_1 e^{q_2 \theta} \quad (23)$$

where

$$q_1 = q_3 + q_4 A_\theta \quad (24)$$

and q_2 , q_3 and q_4 are constants. A_θ is described by Eqns. 11 to 13. A comparison of this model (Eqns. 23 and 24) with test data [39] is displayed in Fig. 8.

For austenite, the yield stress is assumed to be half that of martensite. For the weld metal, an overmatched material is assumed with a yield stress 50 MPa higher than the parent metal. For a mixed-phase material, the yield stress is defined using a rule-of-mixtures approach [27]. The temperature-dependent yield stress, k , based on test data [31], is:

$$k = \sigma_y^0 + q_5 T + q_6 \sigma_y^0 T \quad (25)$$

where q_5 and q_6 are constants. The identified set of parameters for the yield stress model is shown in Table 4.

The kinematic back-stress tensor takes the form of a Taylor-type hardening:

$$\chi = (aMGb\sqrt{\rho})\mathbf{n} \quad (26)$$

where a is a constant, M is the Taylor factor, G is the shear modulus of the material, b is the magnitude of the Burgers vector, ρ is the dislocation-density and \mathbf{n} is the tensor normal to the yield surface:

$$\mathbf{n} = \frac{\boldsymbol{\sigma}'}{\sigma_{eq}} \quad (27)$$

where σ_{eq} is von Mises equivalent stress [45]. Dislocation-density evolution is described as follows [44]:

$$\dot{\rho} = \frac{\rho_0 \dot{\rho}}{(1 - \bar{\rho})^2} \quad (28)$$

where ρ_0 is the initial dislocation density. The value of ρ_0 (see Table 4) was identified here by solving the equation $\sigma_y = aMGb\sqrt{\rho_0}$. The identified value sits within the range of

measured or previously published values, ranging from $7.9 \times 10^7 \text{ mm}^{-2}$ [46] to $9 \times 10^8 \text{ mm}^{-2}$ [2]. $\bar{\rho}$ is the normalised dislocation-density [44]:

$$\bar{\rho} = 1 - \frac{\rho_0}{\rho} \quad (29)$$

which evolves during plastic deformation, as follows:

$$\dot{\bar{\rho}} = g_1(\bar{\rho}_L - \bar{\rho})|\dot{p}| \quad (30)$$

where g_1 and $\bar{\rho}_L$ are both dependent on temperature and phase. In the martensite (tempered or newly-formed) phase, they are defined using double-sigmoid equations (see Appendix for detail). The kinematic back-stress was calibrated against monotonic data from Yaghi et al. [31] across a range of temperatures for three material phases (tempered and newly-formed martensite and austenite), as shown in Fig. 9. For mixed-phase material, e.g. when the material has partially transformed to austenite from martensite, a rule-of-mixtures approach is used to determine the values of g_1 and $\bar{\rho}_L$, following the method described elsewhere [27].

Physically, the isotropic softening model is intended to represent dislocations leaving the centre of the microstructure features such as PAGs, packets or blocks to go to the boundaries where they are annihilated during kinematic hardening (see Appendix). The isotropic hardening variable R is defined as follows:

$$R = aMGb\sqrt{\rho_{cyc}} \quad (31)$$

based on the introduction of a ‘cyclic’ value of dislocation density, defined as the change in value from one cycle to the next. The evolution of ρ_{cyc} is defined as follows:

$$\Delta\rho_{cyc} = \frac{\rho_0\Delta\bar{\rho}_{cyc}}{(1 - \bar{\rho}_{cyc})^2} \quad (32)$$

and the normalised value is:

$$\bar{\rho}_{cyc} = 1 - \frac{\rho_0}{\rho_{cyc}} \quad (33)$$

The normalised, cyclic dislocation-density evolution follows a similar form to Eqn. 28 but rather than a dependency on plastic strain-rate, the accumulated normalised dislocation-density within one half-cycle of plasticity is used:

$$\Delta\bar{\rho}_{cyc} = g_{1c}(\bar{\rho}_{Lc} - \bar{\rho}_{cyc})\Delta\bar{\rho} \quad (24)$$

where

$$g_{1c} = n_4 g_1 \quad (35)$$

and

$$\bar{\rho}_{Lc} = n_5 \bar{\rho}_L e^{n_6 T} \quad (36)$$

with n_4 , n_5 and n_6 as constants. The model was calibrated against cyclic test data for parent metal P91 [47] at a range of strain-ranges and temperatures (Fig. 10). The model parameters for isotropic softening are displayed in Table 4. In Fig. 11, a sample comparison is made between the model and separate high-temperature cyclic test data [48] for P91 at 600°C and a strain-rate of 0.1% s⁻¹.

Damage initiation is represented using a damage-indicator parameter that is based on cyclic softening. Damage is defined to initiate when $R > Q$, where Q is found to be well-represented by a constant value, based on calibration against P91 PM test data across a range of temperatures and strain-ranges [47]. In Fig. 10, damage growth is represented by an equation of the form $\dot{D} = a_1 |\dot{p}|$ to simulate the rapid reduction in stress near the end of uniaxial specimen life. For the current work, attention is focused on prediction of damage-initiation

The non-linear visco-plastic constitutive equations are solved iteratively using the Newton-Raphson method within the UMAT, following a similar approach to that described in detail by the authors previously [27].

2.7 Prediction of in-service flexible operation response of welded joint

After welding, in-service pressure and temperature loading is applied [49], as inferred from power plant flexible operational cycles, each lasting 57 hours, as described in Fig. 12. **A closed-end condition for the pipe was assumed. Investigations into the issue that prompted the early removal of the component from service determined that system stresses were not a significant contributor to the overall stress state. The hanger systems and pipework supports were all functioning as per design, minimising bending or torsional stresses [50].** For computational expediency, only 25 cycles are simulated. Due to the occurrence of continuous cyclic softening, a linear extrapolation from the 25-cycle result is implemented to infer a damage-initiation time for each material point.

The purpose of a weld design tool is to optimise the welding process to improve the predicted service life of components. To illustrate this capability, four different welding

processes with different preheat and inter-pass (PHIP) or PWHT temperatures were simulated, as described in Table 1. For Case A, a PHIP temperature of 350°C with a PWHT temperature of 750°C is used; for Case B, the former is increased to 400°C whilst for Case C the PWHT time is increased to 780°C. These cases allow assessment of the relative effects of these two process temperatures. In each case, the PWHT duration at peak temperature was 70 minutes. Cases A, B and C were all modelled without welding residual stress (WRS). This was intended to isolate the effects of microstructure on in-service performance. An additional case, Case D, was modelled under the same conditions as Case A, but with WRS effects included.

3. Results

3.1 Validation

In order to validate the present methodology, predicted life for cross-welded HTLCF specimens is compared to test data from Shankar et al. [6], for a temperature of 600°C and a strain-range of 2%. Only short PWHT times were simulated due to the significant computational run-times for longer PWHT times. These PWHT results are presented in Fig. 13 in terms of weld life reduction factor ($WLRF = N_f^{PM} / N_f^{CW}$) as a function of PWHT time. In Fig. 13, a power-law equation has been fitted to this short-term data to allow extrapolation to the significantly longer-term PWHT time of the test data. This projection gives a WLRF of 1.269, which is almost identical to the measured value of 1.27. Even without the extrapolation to longer PWHT times, it is clear that the model would give a close prediction of about 1.4 for the WLRF.

3.2 Effect of welding and PWHT processes on microstructure variables

Figures 14a to 14h show the predicted distributions of lath-width, hardness and carbide diameter and area fraction for the as-welded and PWHT conditions for the Case A process. Figure 15 shows the predicted PAG size distribution for both the as-welded and PWHT conditions for Case A, facilitating demarcation of the idealised CGHAZ, FGHAZ and ICHAZ zones (the model also predicts a mixed tempered-untreated martensite phase composition for the ICHAZ, further facilitating demarcation). PWHT is predicted to have no effect on the PAG evolution. Although not shown here, the corresponding results for

Cases B and C are similar to those of Case A, although the maximum and minimum values differ from case to case, as shown in Table 5. Table 5 also includes the corresponding results for Case D, which includes residual stress effects.

3.3 Effect of in-service loading and welding process on stress and microstructure distributions

Figure 16 shows an example of stress redistribution for the Case A radial, axial and hoop stresses between the 1st and 25th in-service cycles steam pressure-temperature cycles. The 1st cycle sample point is at 20,000 seconds of cycle-time, corresponding to the first dwell (616°C and 12.5 MPa). The stress re-distribution is attributed to accumulation of plastic deformation and cyclic softening, due to the high temperature, cyclic viscoplastic behaviour of the material, which is, of course, affected by the microstructure evolution, especially the carbide precipitates. Some key observations on these results are as follows:

- The radial stress distribution (Figs. 16a, 16b) is, of course, dominated by the internal pressure on the inside surface, and is not significantly affected by the cyclic re-distribution, although local tensile stress concentrations develop on the outside surface at the HAZ-WM interface and compressive stress concentrates further in the CGHAZ near the inside surface.
- Significant redistribution of tensile axial stress concentrations (Fig. 16c, 16d) occurs from the inside surface WM-HAZ-PM interfaces to the WM-HAZ interface on the outside surface, with a significantly increased maximum tensile value for the 25th cycle.
- Significant re-distribution of the tensile hoop stresses (which are the dominant stress component) is also predicted (Fig. 16e, 16f) with the tensile stress concentration moving from the inside surface HAZ-WM interface to the inside surface IC-FGHAZ. The peak values of tensile hoop stress reduce slightly.

Fig. 16g shows the precipitate diameter distribution after 25 cycles. Comparing this to Fig. 14f, and also referring to the data in Table 6, it is clear that dramatic precipitate coarsening has occurred in all regions, from between 85 to 100 nm to between 268 to 305

nm, with particular concentration of coarsening in the regions of hoop stress concentration. The results for Cases B and C are generally similar in value and distributions to those of Case A (shown in Figure 14). Figure 17 shows the corresponding predicted distributions for Case D, which exhibits significantly different distributions to those of Cases A to C. In particular, these distributions are significantly more inhomogeneous due to the presence of WRS. Furthermore, significantly larger tensile hoop, radial and axial localised stresses are predicted for this case. Particularly high tensile hoop stresses of about 104 MPa are predicted after 25 cycles in the FGHAZ towards the pipe mid-thickness.

3.4 Effect of in-service loading and welding process on predicted crack initiation

In Figs. 16f and 17f, it is clear that the hoop stresses, which are the dominant stress components, localise in the HAZ. The predicted damage initiation times for the four cases are compared in Fig. 18. The minimum damage initiation life is 4,845 hours, approximately half a year. This damage-initiation life occurred in Case C.

4. Discussion

The use of sequentially-coupled thermal and mechanical analysis is well-established [29, 31, 51, 52]. The use of 24 weld passes was justified by the fact that the pipe was 36 mm thick and typical welding rods for the MMA process have a diameter of 3.2 mm. However, depending on the weld operator, fewer or greater numbers of passes could be used. Even if 24 is not the optimum number, it serves to demonstrate the through-process and weld optimisation capability of the entire model.

The mechanical model, which is physically-based, with dislocation-density as a key state-variable, uses the well-established hyperbolic sine visco-plastic flow-rule with Taylor hardening and cyclic softening. The mechanical model was calibrated against tensile and cyclic data across a range of temperatures and strain-ranges. The method by which kinematic and isotropic hardening define separate dislocation densities for grain boundaries and interiors, in principle, follows the methodology pursued in crystal-plasticity models [53]. The calibration results, displayed in Figs. 9 and 10 are in agreement with the test data and Fig. 11 shows validation of the model, particularly for later fatigue cycles.

The use of a precipitate-based yield stress is consistent with other work [54, 55] and the validation of the model (Fig. 8) reveals a close correspondence to test data.

The microstructure predictions between the as-welded and PWHT cases are shown for Case A in Figs. 14 and 15. The general trends for Case A are the same for Cases B and C, as follows:

- The WM and HAZ contain narrow laths (Figs. 14a, 14b), consistent with newly-formed martensite. The laths widen after PWHT, consistent with the effect of tempering.
- The peak hardness (Figs. 14c, 14d) in the as-welded WM is large, almost twice that of the PM. After PWHT, the peak hardness reduces significantly and the difference between the peak WM hardness and PM hardness also reduces. Physically, this represents the tempering effect of reducing and homogenising hardness in a welded joint.
- The diameter (Figs. 14e, 14f) and area fraction (Figs. 14g, 14h) of carbides is low in the WM after welding, consistent with newly-formed martensite. At high temperature, e.g. during welding, precipitates dissolve [40]. PWHT increases the diameter and area fraction. The diameters become significantly more homogeneous after PWHT. There is a region close to the HAZ with an increased diameter, which is consistent with the IC-HAZ and the associated over-coarsened carbides.
- The PAG sizes (Fig. 15) reveal an unaffected PM region furthest from the WM, with a band of small PAGs which then increase in size with increasing distance into the WM, where the largest PAGs can be found. The largest PAGs correspond to the final weld pass due to a slower cooling rate. PWHT had no effect on PAG sizes.

Comparing Cases A, B and C, it is clear from the results of Table 5 that the increased PWHT temperature of Case C had the greatest effect on the welded microstructure. Preheat and inter-pass temperature did not have a significant effect. This indicates that PWHT is a major determining factor for the final microstructure configuration. The results of a higher PWHT temperature led to the expected effects of extra tempering, including reduced hardness, increased lath width and an increased area fraction of carbide precipitates. In fact, Case C has localised regions of hardness that are

below the ASTM335 limit of 196 HV (Case C had 194 HV) for P91. For the purposes of the current work, the authors do not consider a difference of 2 HV to significantly affect the results or conclusions. The inclusion of WRS led to an increase in the precipitate diameters in the IC-FGHAZ region after PWHT, e.g. compare Fig. 14f to Fig. 17g. This is consistent with observed increases in precipitate diameter in the HAZ near the PM-HAZ interface (e.g. the IC-FGHAZ) after PWHT [43].

The stress localisation displayed in Figs. 9 and 10 and in Table 6 demonstrates clearly the utility of microstructure-sensitive modelling. Not only did welding-induced material heterogeneity lead to stress localisation but the material heterogeneity itself evolved under in-service conditions. The stress heterogeneity (gradients) in Cases A, B and C were similar during the first in-service cycle but after 25 cycles, Case C exhibited markedly greater stress heterogeneity, with higher tensile stresses, compared to Cases A and B. In Case D, the WRS significantly increased the stress heterogeneity as well as the peak tensile stresses for the radial and hoop stresses, although the increase in peak axial stress was less significant. The WRS also changed the location of the hoop stress localisation from the inside surface to a sub-surface region.

To the author's knowledge, this is the first time that through-process modelling of microstructure effects has been incorporated into damage initiation predictions for welded P91 in a realistic geometry. Some authors, without considering through-process effects or even explicitly modelling HAZ, have predicted failure lives based on a limited number of operational cycles in realistic geometries. For example, Farragher et al. [56] used the Ostergren equation, albeit with a two-layer viscoplasticity model, and without explicit incorporation of HAZ and WM behaviour. Li et al. [24] presented a ductility exhaustion life prediction method for three-material PM-HAZ-WM model of a tee-joint, but did not include temperature-dependent material properties or strain-rate effects. Li et al. [57] presented a strain-based fatigue indicator parameter, including triaxiality effects, within a crystal plasticity model for parent material P91. Kyaw et al. [17] presented an energy-based damage-initiation model, but it was calibrated only against PM at a single temperature. Basirat et al. [58] presented a continuum damage model based on solid solution concentration, precipitate coarsening and void nucleation, but the application of this model was creep of PM P91. The present work implements a cyclic-softening fatigue indicator

parameter for damage initiation. Some comments on the predicted damage initiation results of Figure 18 are as follows:

- Clearly, the ICHAZ or PM adjacent to ICHAZ is consistently predicted to be critical location for fatigue damage. This is consistent with observed cracks in welded components, e.g. Type-IV cracking [59].
- Significant damage initiation is predicted within 45,000 hours (about 5 years) for all cases; for Case C, damage initiation is predicted particularly early, within about 4,850 hours, or 85 in-service cycles (about half a year).
- The CGHAZ and WM are predicted to be less critical for damage initiation within the first 45,000 hours.
- For Cases A to C, damage-initiation is predicted to occur at the inside surface of the pipe whereas for Case D, islands of damage-initiation regions are predicted first away from the surface. This indicates that WRS causes initiation of multiple sub-surface cracks, with inevitable coalescence, as opposed surface crack initiation and propagation into the surface.

For the case without WRS, Case B is predicted to have the longest time to crack initiation whereas Case C is predicted to have the shortest time (in the ICHAZ). This is attributable to: (a) the higher PWHT temperature of Case C causing increased tempering, and hence slight coarsening of the precipitates and significantly increased precipitate area fraction (see Table 5), leading to a softer material and increased cyclic softening and (b) the higher PHIP temperature of Case B extending the width of the HAZ into the PM, resulting in a larger region of harder material.

Figure 18 indicates that WRS is detrimental to in-service performance. The damage-initiation region for Case A is at the inside surface of the pipe and does not extend far through the wall thickness. For Case D, the damage initiation regions are more numerous and extend deeper below the pipe surface. These multiple sub-surface cracks correspond to the tensile hoop stress localisation zones (Fig. 17f). Such interior cracks might not be detectable by plant operators whereas surface cracks could be detected and treated, either by repairing or replacing the pipe.

Even though the applied steam pressure of less than 13 MPa is relatively low, it is important to note that the present methodology predicts damage initiation, which typically pertains to very small cracks (less than 200 μm , based on experimentally-observed correlation between HTLCF for P91 and crack-length in a thick-walled pipe from Okamura et al. [60]), as opposed to pipe fracture. Recent plant experience has indicated the detection of premature cracking within similar time-scales to those predicted here, e.g. a tee-joint that failed under similar conditions to those simulated here after only about 8,000 hours [61].

Conclusions

A microstructure-based, through-process model, using a sequential thermomechanical simulation methodology, was applied to a representative, finite-element, welded pipe geometry to predict the effects of multi-pass welding and post-weld heat-treatment on the in-service performance of welded power plant components under representative flexible-operational conditions. Key conclusions are as follows:

- Welding was predicted to produce (i) large prior austenite grains in the weld metal, (ii) a fine-grained heat-affected zone in the parent metal offset from the fusion line and (iii) newly-formed martensite in the weld metal and heat-affected zone, all consistent with observed experimental trends [62].
- Post-weld heat treatment was predicted to (i) equalise the microstructure, (ii) reduce peak hardness and (iii) increase lath-width, precipitate size and area fraction, again all consistent with observed results for tempering of 9Cr steel [63].
- Significant stress redistribution was predicted to occur during in-service loading, with stress concentrating in the heat-affected zone of the weld.
- Higher post-weld heat treatment temperature led to a softer, more tempered material, consistent with experimental observations [38], giving reduced initiation life.
- Cyclic-softening damage was predicted to occur earliest in either the inter-critical heat-affected zone or in the neighbouring parent metal, consistent with cracking in cross weld specimens under HTLCF conditions [5, 6].

Acknowledgements

This research is funded by Science Foundation Ireland grant numbers SFI/14/IA/2604 and SFI/16/RC/3872. The authors would like to acknowledge the contributors to this research; NUI Galway, the Ryan Institute, General Electric (UK), ESB International, University of Limerick, Imperial College London, I-Form, Ireland and Fraunhofer IWM, Freiburg. The authors would also like to thank Mr. S. Scully (ESB International) for supplying load-following plant temperature and pressure data for use in this work.

Nomenclature

a	Multiplicative constant (kinematic back-stress, cyclic softening)
a_1	Multiplicative constant (cyclic damage model)
A_{c1}	Austenite transformation-start temperature
A_{c3}	Austenite transformation-finish temperature
A_θ	Area-fraction of precipitates
b	Magnitude of Burgers vector
C	Multiplicative constant (Ostergren equation)
CF	Creep-fatigue
c_1	Multiplicative constant (grain recrystallisation model)
c_2	Multiplicative parameter (grain growth model)
c_3, c_4	Multiplicative constants (grain growth model)
d	PAG size
d_{\min}	Minimum PAG size
D	Damage
f	Plastic yield function
FGHAZ	Fine-grained HAZ
G	Shear modulus (kinematic back-stress, cyclic softening)
g_1	Multiplicative parameter (normalised dislocation-density model)
g_{1c}	Multiplicative parameter (cyclic softening model)
g_2, g_3	Multiplicative constants (normalised dislocation-density model)
H	Vickers hardness
H_L	Asymptotic Vickers hardness
HTLCF	High-temperature, low-cycle fatigue
HAZ	Heat-affected zone
ICHAZ	Intercritical heat-affected zone
$J_p, J_s, J_f, J_{r1}, J_{r2}, J_{T1},$	Multiplicative constants (normalised dislocation-density model)
J_{T2}	
k	Temperature-dependent yield stress
L	Lath-width
L_{Lim}	Asymptotic lath-width (lath-width model)
m_1	Multiplicative parameter (area-fraction model)
m_2, m_3, m_4	Multiplicative constants (area-fraction model)
$m_5, m_6, m_7, m_8, m_9,$	Multiplicative constants (precipitate-diameter model)
m_{10}	
M_s	Martensite transformation-start temperature
M	Taylor factor (kinematic back-stress, cyclic softening)
MMA	Manual metal arc
n	Direction tensor
n_1	Multiplicative constant (area-fraction model)
n_2	Multiplicative constant (precipitate-diameter model)
n_3	Multiplicative constant (visco-plastic flow rule)

n_4, n_5, n_6	Multiplicative constants (cyclic softening model)
p	Plastic multiplier
PAG	Prior-austenite grain
$P_p, P_s, P_f, P_{r1}, P_{r2}$	Multiplicative parameters (normalised dislocation-density model)
$P_{T1}, P_{T2}, P_s^Y, P_{r1}^Y, P_{T1}^Y$	Multiplicative constants (normalised dislocation-density model)
PM	Parent metal
PHIP	Preheat and inter-pass
PWHT	Post-weld heat treatment
Q	Cyclic-softening threshold
q_1	Multiplicative parameter (yield stress model)
q_2, q_3, q_4, q_5, q_6	Multiplicative constants (yield stress model)
R	Taylor hardening parameter
S	Recrystallised volume fraction
T	Temperature
TMF	Thermomechanical fatigue
UMAT	User-material subroutine
V_γ	Volume fraction of austenite
$V_{\alpha'}$	Martensite volume-fraction
WLRF	Weld life reduction factor
WM	Weld metal
α	Multiplicative parameter (viscoplastic flow rule)
β	Multiplicative constant (viscoplastic flow rule)
β_2	Multiplicative constant (Ostergren equation)
χ	Kinematic back-stress tensor
$\Delta\varepsilon_{\alpha'}$	Transformation strain (martensite transformation)
$\Delta\varepsilon_\gamma$	Transformation strain (austenite transformation)
λ	Multiplicative constant (martensite transformation)
λ_2, λ_3	Multiplicative constant (phase transformation strain)
μ_1	Multiplicative parameter (hardness model)
$\mu_2, \mu_3, \mu_4, \mu_5$	Multiplicative constants (hardness model)
$\mu_6, \mu_7, \mu_8, \mu_9$	Multiplicative constants (lath-width model)
θ	Precipitate diameter
ρ	Dislocation-density
ρ_0	Initial dislocation-density
$\bar{\rho}$	Normalised dislocation-density
$\bar{\rho}_L$	Asymptotic normalised dislocation-density (normalised dislocation-density model)
ρ_{cyc}	Cyclic dislocation-density
$\bar{\rho}_{cyc}$	Normalised cyclic dislocation-density
$\bar{\rho}_{Lc}$	Asymptotic normalised cyclic dislocation-density (cyclic softening model)
σ_y	Yield stress
σ'	Deviatoric stress tensor

σ_y^0	Room-temperature yield stress
σ_{eq}	Von Mises equivalent stress
9Cr	9% chromium

References

1. Abe, F., *Research and Development of Heat-Resistant Materials for Advanced USC Power Plants with Steam Temperatures of 700 °C and Above*. Engineering, 2015. **1**: p. 211-224.
2. Ennis, P.J., Czyska-Filemonowicz, A., *Recent Advances in Creep Resistant Steels for Power Plant Applications*. Operation Maintenance and Materials Issue, 2002. **1**(1).
3. Sauzay, M., Brillet, H., Monnet, I., Mottot, M., Barcelo, F., Fournier, B., Pineau, A., *Cyclically induced softening due to low-angle boundary annihilation in a martensitic steel*. Materials Science and Engineering A, 2005. **400-401**: p. 241-244.
4. Francis, J.A., Mazur, W., Bhadeshia, H. K. D. H., *Type IV cracking in ferritic power plant steels*. Materials Science and Technology, 2006. **22**(12): p. 1387-1395.
5. Farragher, T.P., Scully, S., O'Dowd, N. P., Hyde, C. J., Leen, S. B., *High Temperature, low cycle fatigue characterisation of P91 weld and heat affected zone material*. Journal of Pressure Vessel Technology, 2014. **136**: p. 021403-1 - 021403-10.
6. Shankar, V., Sandhya, R., Mathew, M.D., *Creep-fatigue-oxidation interaction in Grade 91 steel weld joints for high temperature applications*. Materials Science and Engineering A, 2011. **528**: p. 8428-8437.
7. Hyde, T.H., Sun, W., Becker, A. A., *Analysis of the impression creep test method using a rectangular indenter for determining the creep properties in welds*. International Journal of Mechanical Sciences, 1996. **38**: p. 1089-1102.
8. Hyde, C.J., Hyde, T. H., Sun, W., Nardone, S., De Bruycker, E., *Small ring testing of a creep resistant material*. Materials Science and Engineering A, 2013. **586**: p. 358-366.
9. Hyde, C.J., Sun, W., *Evaluation of conversion relationships for impression creep test at elevated temperatures*. International Journal of Pressure Vessels and Piping, 2009. **86**: p. 757-763.
10. Tao, J.X.Y., Rayner, G., *Creep Fatigue Crack Initiation Assessment for Weldment Joint Using the Latest R5 Assessment Procedure*. Procedia Engineering, 2015. **130**: p. 879-892.

11. Hyde, T.H., Saber, M., Sun, W., *Creep crack growth data and prediction for a P91 weld at 650 °C*. International Journal of Pressure Vessels and Piping, 2010. **87**: p. 721-729.
12. Perrin, I.J., Hayhurst, D. R., *Continuum damage mechanics analyses of type IV creep failure in ferritic steel crossweld specimens*. International Journal of Pressure Vessels and Piping, 1999. **76**: p. 599-617.
13. Hayhurst, R.J., Mustata, R., Hayhurst, D. R., *Creep constitutive equations for parent, Type IV, R-HAZ, CGHAZ and weld material in the range 565-640°C for Cr-Mo-V weldments*. International Journal of Pressure Vessels and Piping, 2005. **82**: p. 137-144.
14. Hyde, T.H., Sun, W., Becker, A. A., *Effect of geometry change on the creep failure life of a thick-walled CrMoV pipe with a circumferential weld*. International Journal of Pressure Vessels and Piping, 2004. **81**: p. 363-371.
15. Touboul, M., Crepin, J., Rousselier, G., Latourte, F., Leclercq, S., *Identification of Local Viscoplastic Properties in P91 Welds from Full Field Measurements at Room Temperature and 625 °C*. Experimental Mechanics, 2013. **53**: p. 455-468.
16. Fournier, B., Sauzay, M., Pineau, A., *Micromechanical model of the high temperature cyclic behaviour of 9-12%Cr martensitic steels*. International Journal of Plasticity, 2011. **27**: p. 1803-1816.
17. Kyaw, S.T., Rouse, J. P., Lu, J. Sun, W., *Determination of material parameters for a unified viscoplasticity-damage model for a P91 power plant steel*. International Journal of Mechanical Sciences, 2016. **115-116**: p. 168-179.
18. A. Benaarbia, J.P.R., W. Sun, *A thermodynamically-based viscoelastic-viscoplastic model for the high temperature cyclic behaviour of 9-12% Cr steels*. International Journal of Plasticity, 2018. **107**: p. 100-121.
19. Rouse, J.P., Sun, W., Hyde, T. H., Morris, A., *Comparative assessment of several creep damage models for use in life prediction*. International Journal of Pressure Vessels and Piping, 2013. **108-109**: p. 81-87.
20. Hyde, T.H., Becker, A. A., Sun, W., Williams, J. A., *Finite-element creep damage analyses of P91 pipes*. International Journal of Pressure Vessels and Piping, 2006. **83**: p. 853-863.
21. Khayatzaheh, S., Tanner, D. W. J., Truman, C. E., Flewitt, P. E. J., *Creep deformation and stress relaxation of a martensitic P92 steel at 650°C*. Engineering Fracture Mechanics, 2017. **175**: p. 57-71.

22. Ó Murchú, C.L., S. B., O'Donoghue, P., Barrett, R. A., *A precipitate evolution-based continuum damage mechanics model of creep behaviour in welded 9Cr steel*. Journal of Materials Design and Applications, 2018.
23. Hyde, T.H., Sun, W., *A method for estimating the stress distributions on the centre line of an axisymmetric, Two-material, cross-weld, creep test specimen*. International Journal of Mechanical Sciences, 1997. **39**: p. 885-898.
24. Li, M., Barrett, R. A., Scully, S., Harrison, N. M., Leen, S. B., O'Donoghue, P. E., *Cyclic plasticity of welded P91 material for simple and complex power plant connections*. International Journal of Pressure Vessels and Piping, 2016. **87**: p. 391-404.
25. Hall, F.R., Hayhurst, D. R., *Continuum Damage Mechanics Modelling of High Temperature Deformation and Failure in a Pipe Weldment*. Proceedings: Mathematical and Physical Sciences, 1991. **433**: p. 383-403.
26. Hayhurst, D.R., Hayhurst, R. J., Vakili-Tahami, F., *Continuum damage mechanics predictions of creep damage initiation and growth in ferritic steel weldments in a medium bore branched pipe under constant pressure at 590°C using a five-material weld model*. Proceedings of the Royal Society A, 2005. **461**: p. 2303-2326.
27. Mac Ardghail, P., Harrison, N., Leen, S. B., *A through-process, thermomechanical model for predicting welding-induced microstructure evolution and post-weld high-temperature fatigue response*. International Journal of Fatigue, 2018. **112**: p. 216-232.
28. Deng, D., Murakawa, H., *Prediction of welding residual stress in multi-pass butt-welded modified 9Cr-1Mo steel pipe considering phase transformation effects*. Computational Materials Science, 2006. **37**: p. 209-219.
29. Yaghi, A.H., Hyde, T. H., Becker, A. A., Williams, J. A., Sun, W., *Residual stress simulation in welded sections of P91 pipes*. Journal of Materials Processing Technology, 2005. **167**: p. 480-487.
30. Rouse, J.P., Hyde, C. J., Morris, A., *A neural network approach for determining spatial and geometry dependent Green's functions for thermal stress approximation in power plant header components*. International Journal of Pressure Vessels and Piping, 2018. **168**: p. 269-288.
31. Yaghi, A.H., Hyde, T. H., Becker, A. A., Sun, W., *Finite element simulation of residual stresses induced by the dissimilar welding of a P92 steel pipe with weld metal IN625*. International Journal of Pressure Vessels and Piping, 2013. **111-112**: p. 173-186.

32. Hamelin, C.J., Muransky, O., Smith, M. C., Holden, T. M., Luzin, V., Bendeich, P. J., Edwards, L., *Validation of a numerical model used to predict phase distribution and residual stress in ferritic steel weldments*. Acta Materialia, 2014. **75**: p. 1-19.
33. Koistinen, D.P., Marburger, R.E, *A general equation prescribing the extent of the austenite-martensite transformation in pure iron-carbon alloys and plain carbon steels*. Acta Metallurgica, 1959. **7**(1): p. 59-60.
34. Vallourec & Mannesmann Tubes, *V & M Experience in T/P91 Tubes and Pipes*, in *International Workshop on Fabrication & Processing of Grade 91 Material, FAB 91/2011*: Tiruchirappalli, India.
35. Cerjak, H., *The Role of Welding in the Power Generation Industry*. Proceedings of the International Conference Safety and Reliability of Welded Components, 2008: p. 17-27.
36. Francis, J.A., Bhadeshia, H. K. D. H., Withers, P. J., *Welding residual stresses in ferritic power plant steels*. Materials Science and Technology, 2007. **23**(9): p. 1009-1020.
37. Milovic, L., Vuherer, T., Blacic, I., Vrhovac, M., Stankovic, M., *Microstructures and mechanical properties of creep resistant steel for application at elevated temperatures*. Materials and Design, 2013. **46**: p. 660-667.
38. Potirniche, G., Charit, I., Rink, K., Barlow, F., *Prediction and monitoring systems of creep-fracture behaviour of 9Cr-1Mo steels for reactor pressure vessels*. NEUP 2009 Project, 2013. **09-835**.
39. Barbadikar, D.R., Deshmukh, G. S., Maddi, L., Laha, K., Parameswaran, P., Ballal, A. R., Peshwe, D. R., Paretkar, R. K., Nandagopal, M., Mathew, M. D., *Effect of normalizing and tempering temperatures on microstructure and mechanical properties of P92 steel*. International Journal of Pressure Vessels and Piping, 2015. **132-133**: p. 97-105.
40. Shen, Y., Liu, H., Shang, Z., Xu, Z., *Precipitate phases in normalized and tempered ferritic/martensitic steel P92*. Journal of Nuclear Materials, 2015. **465**: p. 373-382.
41. Guguloth, K., Swaminathan, J., Roy, N., Ghosh, R. N., *Uniaxial creep and stress relaxation behaviour of modified 9Cr-1Mo steel*. Materials Science and Engineering A, 2017. **684**: p. 683-696.
42. Zielinski, A., Miczka, M., Boryczko, B., Sroka, M., *Forecasting in the presence of microstructural changes for the case of P91 steel after long-term ageing*. Archives of Civil and Mechanical Engineering, 2016. **16**: p. 813-824.

43. Lee, J.S., Maruyama, K., *Mechanism of Microstructural Deterioration Preceding Type IV Failure in Weldment of Mod.9Cr-1Mo Steel*. Metallurgical Materials International, 2015. **21**: p. 639-645.
44. Li, H., Lin, J., Dean, T. A., Wen, S. W., Bannister, A. C., *Modelling mechanical property recovery of a linepipe steel in annealing process*. International Journal of Plasticity, 2009. **25**: p. 1049-1065.
45. Dunne, F., Petrinic, N., *Introduction to Computational Plasticity* 2005: Oxford University Press.
46. Li, M., Wang, L., Almer, J. D., *Dislocation evolution during tensile deformation in ferritic-martensitic steels revealed by high-energy X-rays*. Acta Materialia, 2014. **76**: p. 381-393.
47. Nagesha, A., Valsan, M., Kannan, R., Bhanu Sanakara Rao, K., Mannan, S. L., *Influence of temperature on the low cycle fatigue behaviour of a modified 9Cr-1Mo ferritic steel*. International Journal of Fatigue, 2002. **24**: p. 1283-1293.
48. Barrett, R.A., O'Donoghue, P. E., Leen, S. B., *A dislocation-based model for high temperature cyclic viscoplasticity of 9-12Cr steels*. Computational Materials Science, 2014. **92**: p. 286-297.
49. Scully, S., *Personal Correspondence*. ESB International, February 2018.
50. Scully, S., *Personal Correspondence*. ESB International, April 2019.
51. Brickstad, B., Josefson, B. L., *A parametric study of residual stresses in multi-pass butt-welded stainless steel pipes*. International Journal of Pressure Vessels and Piping, 1998. **75**: p. 11-25.
52. Yaghi, A.H., Hyde, T. H., Becker, A. A., Sun, W., *Finite element simulation of welding and residual stresses in a P91 steel pipe incorporating solid-state phase transformation and post-weld heat treatment*. Journal of Strain Analysis, 2008. **43**: p. 275-293.
53. Evers, L.P., Parks, D. M., Brekelmans, W. A. M., Geers, M. G. D., *Crystal plasticity model with enhanced hardening by geometrically necessary dislocation accumulation*. Journal of the Mechanics and Physics of Solids, 2002. **50**: p. 2403-2424.
54. Hoang, N.-H., Hopperstad, O. S., Myhr, O. R., Marioara, C., Langseth, M., *An improved nano-scale material model applied in axial-crushing analysis of square hollow section aluminium profiles*. Thin-Walled Structures, 2015. **92**: p. 93-103.

55. Myhr, O.R., Grong, O., Pedersen, K. O., *A combined precipitation, yield strength, and work hardening model for Al-Mg-Si alloys*. Metallurgical and Materials Transactions A, 2010. **41A**: p. 2276-2289.
56. Farragher, T.P., Scully, S., O'Dowd, N. P., Leen, S. B., *Development of life assessment procedures for power plant headers operated under flexible loading scenarios*. International Journal of Fatigue, 2013. **49**: p. 50-61.
57. Li, D.-F., Barrett, R. A., O'Donoghue, P. E., Hyde, C. J., O'Dowd, N. P., Leen, S. B., *Micromechanical finite element modelling of thermo-mechanical fatigue for P91 steels*. International Journal of Fatigue, 2016. **87**: p. 192-202.
58. Basirat, M., Shrestha, T. Potirniche, G. P., Charit, I., Rink, K., *A study of creep behaviour of modified 9Cr-1Mo steel using continuum-damage modelling*. International Journal of Plasticity, 2012. **37**: p. 95-107.
59. Xue, W., Qian-gang, P., Yao-yao, R., Wei, S., Hui-qiang, Z., Hong, L., *Microstructure and type IV cracking behaviour of HAZ in P92 steel weldment*. Materials Science and Engineering A, 2012. **552**: p. 493-501.
60. Okamura, H., Ohtani, R., Saito, K., Kimura, K., Ishii, R., Fujiyama, K., Hongo, S., Iseki, T., Uchida, H., *Basic investigation for life assessment technology of modified 9Cr-1Mo steel*. Nuclear Engineering and Design, 1999. **193**: p. 243-254.
61. Scully, S., *Personal correspondence*. ESB International, December 2018.
62. Pandey, C., Mahapatra, M. M., Kumar, P., Saini, N., *Some studies on P91 steel and their weldments*. Journal of Alloys and Compounds, 2018. **743**: p. 332-364.
63. Lomozik, M., Zielinska-Lipiec, A., *Microscopic analysis of the influence of multiple thermal cycles on simulated HAZ toughness in P91 steel*. Archives of Metallurgy and Materials, 2008. **53**: p. 1025-1034.

Table Caption List

Table 1	A description of the three welding simulation cases.
Table 2	Identified parameters for the phase-transformation and grain-size evolution models.
Table 3	Identified parameters for the hardness and lath evolution models.
Table 4	Identified parameters for the precipitate diameter and area-fraction, unified visco-plasticity constitutive model using combined kinematic-isotropic hardening-softening, and damage and yield-stress evolution models.
Table 5	Comparative microstructure predictions (ranges of values) for the three welding cases after PWHT.

Table 6	Comparative precipitate diameter predictions for the four welding cases for the first and 25th in-service cycles.
Table A.1	Identified parameters for the dislocation-density evolution model.

Figure caption list

Fig. 1	Thermal contour plots for the 24-pass welding simulation for the (a) 1st pass, (b) 9th pass, (c) 13th pass and (d) 22nd pass.
Fig. 2	A schematic of the axisymmetric FE welding geometry (dimensions in mm) with the 24 weld beads labelled, as well as the temperature heating profile associated with each weld bead
Fig. 3	A schematic representation of (a) the temperature history of a material point during a multi-pass welding simulation and (b) the corresponding phase volume fraction history of the same material point. Note that this example corresponds to a mixed-phase, ICHAZ region.
Fig. 4	Calibration of the grain evolution model (line) against test data [37] (points).
Fig. 5	Calibration of the hardness evolution model (lines) against test data [38] (points) for (a) normalising and (b) PWHT conditions.
Fig. 6	Calibration of (a) the asymptotic lath-width (L_{Lim}), based on data from Ennis et al. [2] and (b) the lath-width-hardness relationship, based on data from Barbadikar et al. [39]. Lines represent the model, points represent test data.
Fig. 7	Calibration of the model (lines) against test data (points [2, 39, 41-43]) for (a) the area fraction of precipitates, (b) and (c) the precipitate diameter.
Fig. 8	A comparison between predicted yield stress and test data [39] at room-temperature. The dotted lines represent deviations of 10% from a perfect match.
Fig. 9	Calibration of the material model (lines) against test data [31] (points) for (a) tempered martensite, (b) newly-formed martensite and (c) austenite P92 across a range of temperatures.
Fig. 10	Calibration of the cyclic-softening model against test data [47] at 500°C at strain-ranges of (a) 0.5% and 0.8% and (b) 1.2% and 2%, at a constant strain-rate ($0.3\%s^{-1}$); comparisons between the experimentally-observed [47] and modelled number of cycles to damage initiation (taken as a sudden drop in peak-stress – see Fig.6) for (c) strain-ranges of 0.5%, 0.8%, 1.2% and 2% at different temperatures at a strain-rate of 0.3% (the dotted lines represent deviations of 25% from a perfect match) and (d) sample strain-life results for 500°C.
Fig. 11	A comparison between cyclic data for P91 PM [48] (points) and the current model for the first and 600 th cycle at 600°C, strain-rate 0.1%/s and strain-range 1%.
Fig. 12	The (a) temperature-time and (b) pressure-time histories to which the FE geometry is subjected following welding and PWHT.
Fig. 13	Extrapolation of through-process prediction [27] of WLRF from short-term PWHT times to long-term PWHT times for comparison against long-term PWHT test data with a trend-line projection to experimental WLRF for P91 at 600°C, strain-range 2%, strain-rate 0.3% [6].

Fig. 14	The predicted lath-width [(a) and (b)], Vickers hardness [(c) and (d)], carbide diameter [(e) and (f)] and carbide area fraction [(g) and (h)] results for Case A in the as-welded and PWHT conditions.
Fig. 15	The predicted prior-austenite grain size results for Case A for both the as-welded and PWHT conditions, showing separate predicted HAZ regions
Fig. 16	Predicted stress contour plots for radial (a, b), axial (c, d) and hoop (e, f) for the first dwell period in the 57-hour in-service cycle for the first and 25 th in-service cycles and the precipitate diameter distribution for the 25 th cycle (g) for Case A.
Fig. 17	Predicted stress contour plots for radial (a, b), axial (c, d) and hoop (e, f) for the first dwell period in the 57-hour in-service cycle for the first and 25 th in-service cycles and the precipitate diameter distribution for the first and 25 th cycle for Case D.
Fig. 18	Contour plots of predicted damage initiation times under 45,000 hours for Cases A to D and the contour plot of predicted damage initiation times under 10,000 hours for Case C.

Table 1. A description of the three welding simulation cases.

Case	PHIP temperature (°C)	PWHT temperature (°C)
A	350	750
B	400	750
C	350	780

Table 2. Identified parameters for the phase-transformation and grain-size evolution models.

Parameter	Value
A_{c1}	830 °C, 1103 K
λ	1.2
$\Delta\varepsilon_\gamma$	-0.244 %
A_{c3}	920 °C, 1193 K
M_s	400 °C, 673 K
$\Delta\varepsilon_{\alpha'}$	0.75 %
d_{\min}	1 μm
c_1	0.0071 K ⁻¹
c_3	$2.8 \times 10^{-4} \text{ s}^{-1}$
c_4	$9.45 \times 10^{-3} \text{ K}^{-1}$

Table 3. Identified parameters for the hardness and lath evolution models.

Parameter	Value ($T < 820^\circ\text{C}$)	Value ($T > 820^\circ\text{C}$)
μ_2	$-5 \times 10^{-4} \text{ s}^{-1}$	$-5 \times 10^{-3} \text{ s}^{-1}$
μ_3	$1.15 \times 10^{-6} \text{ s}^{-1}\text{K}^{-1}$	$1.15 \times 10^{-5} \text{ s}^{-1}\text{K}^{-1}$
μ_4	577 kgfmm ⁻²	423 kgfmm ⁻²
μ_5	-0.5 kgfmm ⁻²	0.5 kgfmm ⁻²
μ_6		0.0006 s ⁻¹
μ_7		$-2.25 \times 10^{-6} \text{ mm}^3\text{kgf}^{-1}$
μ_8		38.1 nm
μ_9		0.0032 K ⁻¹

Table 4. Identified parameters for the precipitate diameter and area-fraction, unified visco-plasticity constitutive model using combined kinematic-isotropic hardening-softening, and damage and yield-stress evolution models.

Parameter	Value	Parameter	Value
m_2	1 %	β	0.011 MPa ⁻¹
m_3	-0.026 s ⁻¹	n_3	$3.7 \times 10^{-7} \mu\text{m}^{-1}$
m_4	$4 \times 10^{-5} \text{s}^{-1}\text{K}^{-1}$	n_4	0.0005
n_1	-0.018 %K ⁻¹	n_5	4.91×10^{-7}
m_5	1.5 nm ² s ⁻¹	n_6	0.023 K ⁻¹
m_6	20 nm	a_1	0.14
m_7	3.5	Q	100 MPa
m_8	30 nm	a_2	$2.43 \times 10^{-8} \text{s}^{-1}$
m_9	0.4 nmK ⁻¹	a_3	0.034 MPa ⁻¹
m_{10}	1.3 nmMPa ⁻¹	θ_T	445 nm
n_2	-0.3 nmK ⁻¹	q_2	-0.0022 nm ⁻¹
a	0.33	q_3	1176 MPa
M	3	q_4	-72.73 MPa% ⁻¹
b	0.248 nm	q_5	-0.0773 MPaK ⁻¹
ρ_0	$4.4 \times 10^8 \text{mm}^{-2}$	q_6	-0.00117 K ⁻¹

Table 5. Comparative microstructure predictions (ranges of values) for the three welding cases after PWHT.

Microstructure parameter	Case A	Case B	Case C	Case D
Hv (kgf/mm ²)	206 to 238	206 to 238	194 to 220	206, 238
Lath width (nm)	420 to 643	420 to 643	470 to 673	420, 643
Carbide diameter (nm)	85 to 109	85 to 109	89 to 109	97, 120
Carbide area fraction (%)	5.2 to 7.2	5.2 to 7.2	6.0 to 7.9	5.2, 7.2

Table 6. Comparative precipitate diameter predictions for the four welding cases for the first and 25th in-service cycles.

In-service cycle	Case A θ (nm)	Case B θ (nm)	Case C θ (nm)	Case D θ (nm)
0	85 to 109	85 to 109	89 to 109	97 to 120
25	268 to 305	268 to 304	270 to 307	271 to 319

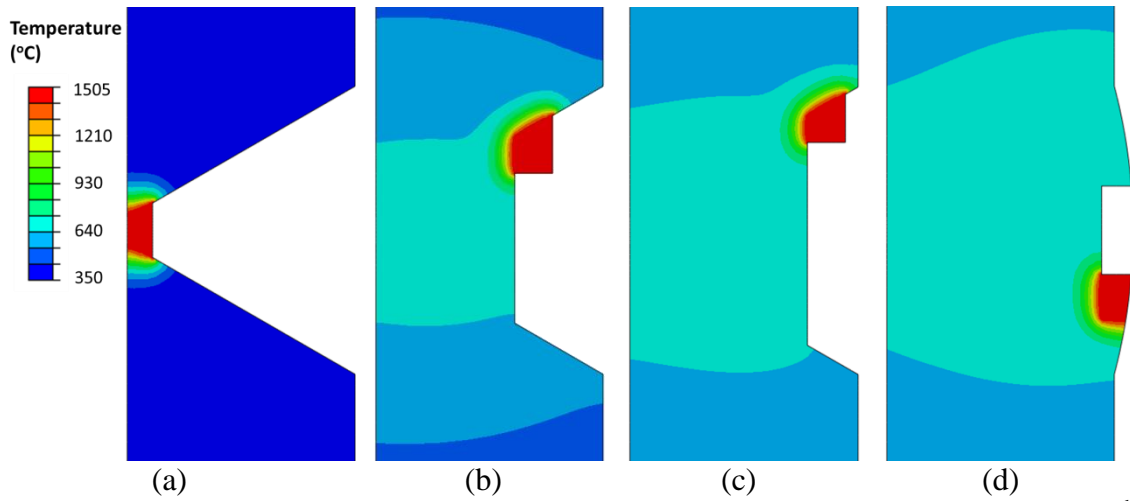


Fig. 1. Thermal contour plots for the 24-pass welding simulation for the (a) 1st pass, (b) 9th pass, (c) 13th pass and (d) 22nd pass.

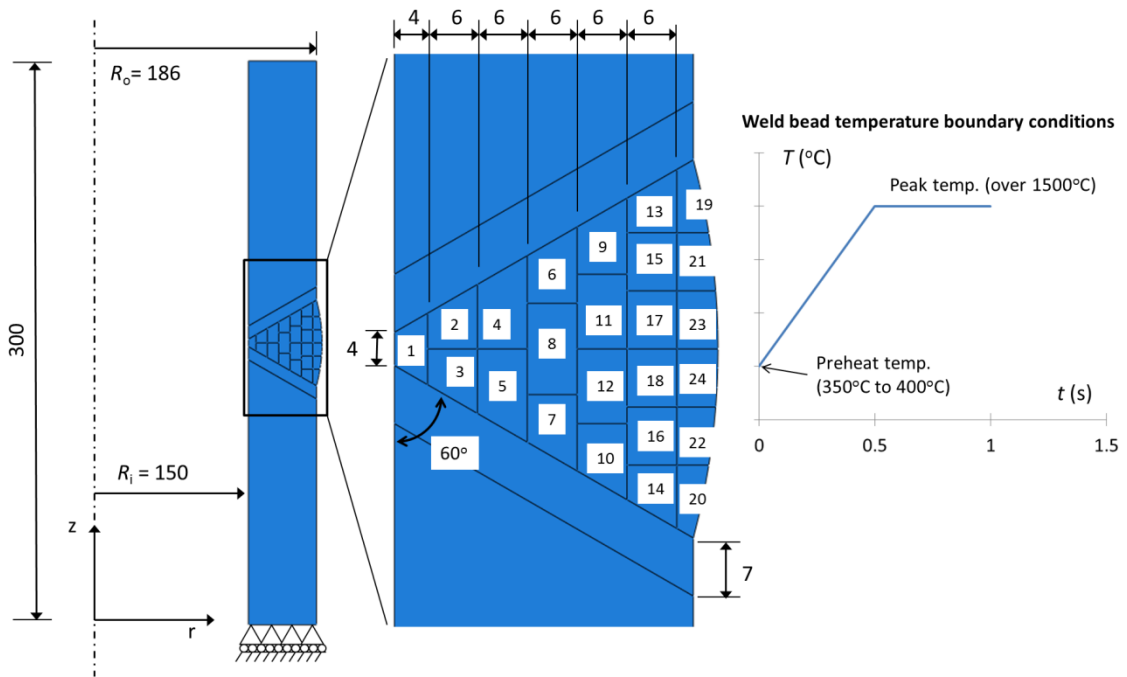
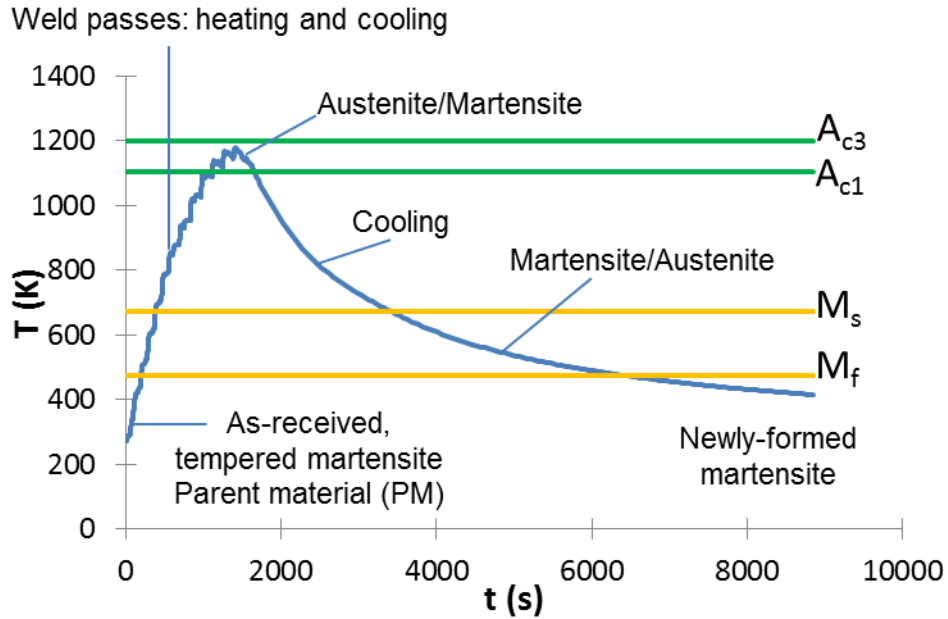
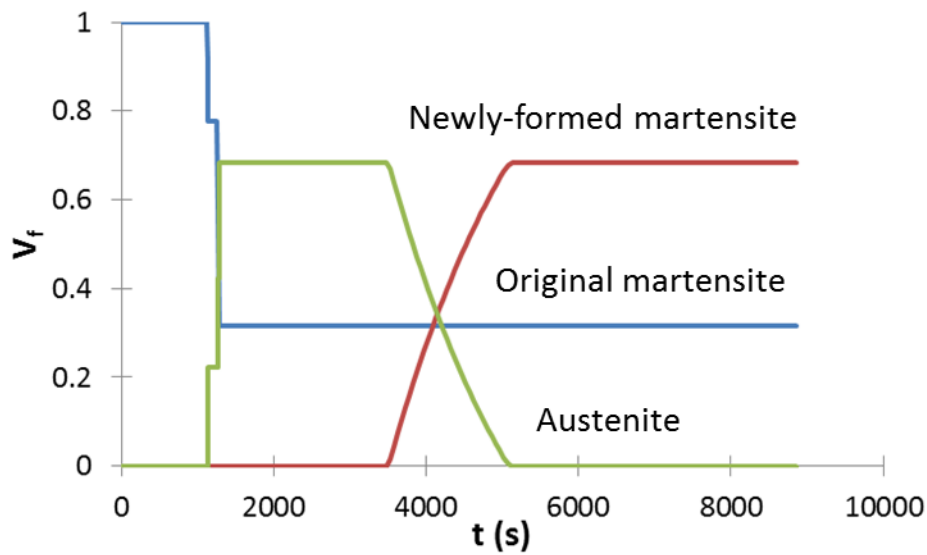


Fig. 2. A schematic of the axisymmetric FE welding geometry (dimensions in mm) with the 24 weld beads labelled, as well as the temperature heating profile associated with each weld bead.



(a)



(b)

Fig. 3. A schematic representation of (a) the temperature history of a material point during a multi-pass welding simulation and (b) the corresponding phase volume fraction history of the same material point. Note that this example corresponds to a mixed-phase, ICHAZ region.

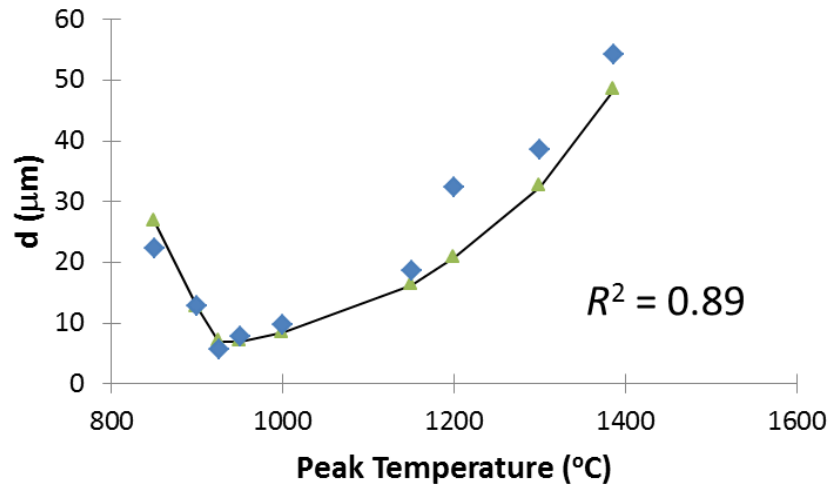
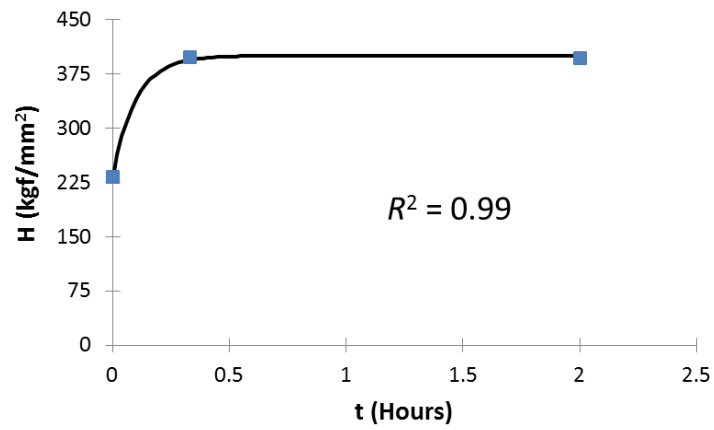
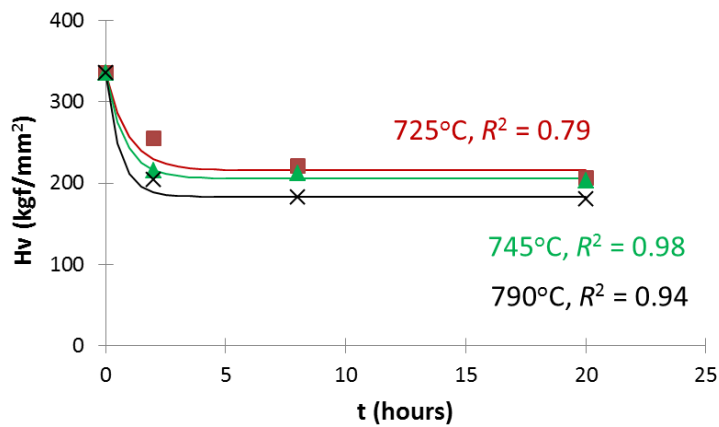


Fig. 4. Calibration of the grain evolution model (line) against test data [37] (points).

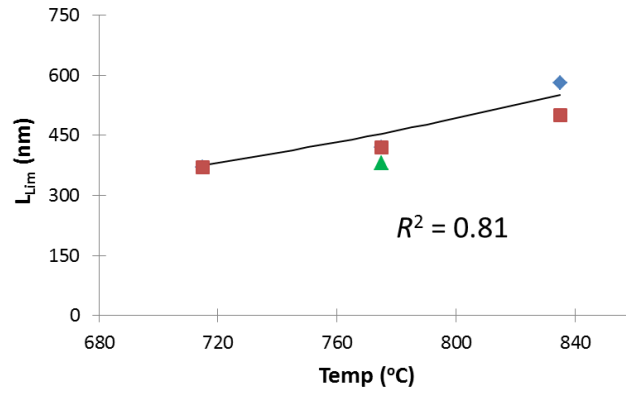


(a)

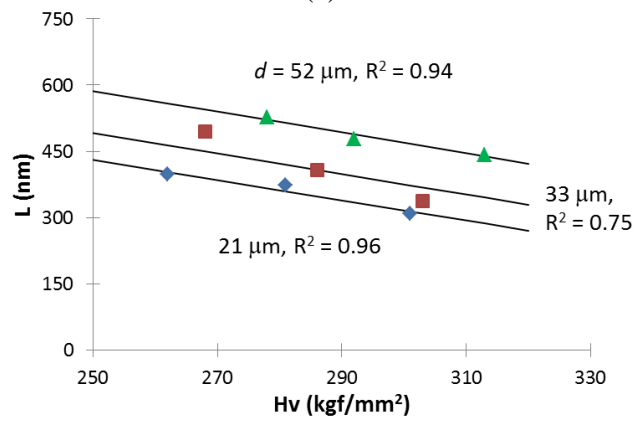


(b)

Fig. 5. Calibration of the hardness evolution model (lines) against test data [38] (points) for (a) normalising and (b) PWHT conditions.

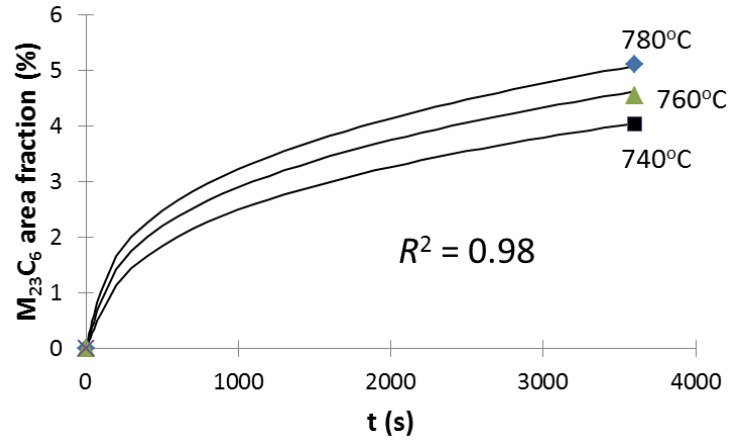


(a)

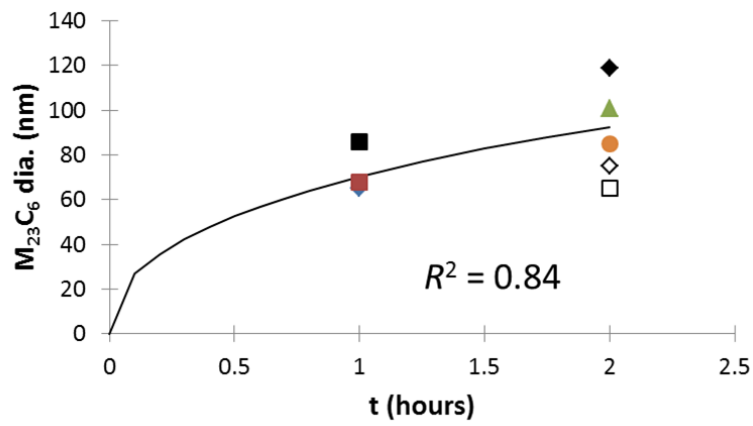


(b)

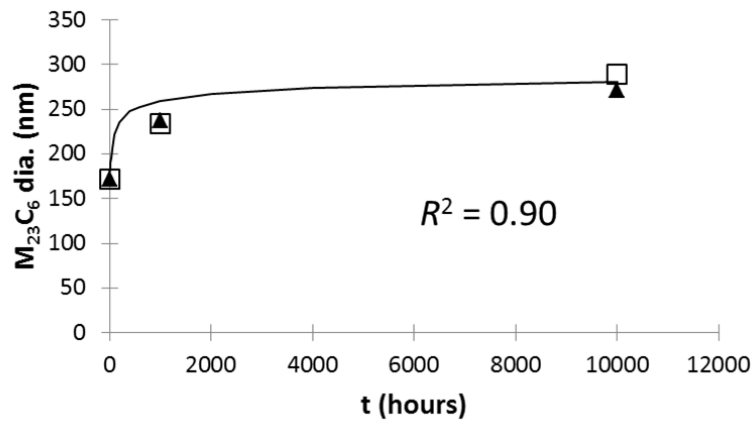
Fig. 6. Calibration of (a) the asymptotic lath-width (L_{Lim}), based on data from Ennis et al. [2] and (b) the lath-width-hardness relationship, based on data from Barbadikar et al. [39]. Lines represent the model, points represent test data.



(a)



(b)



(c)

Fig. 7. Calibration of the model (lines) against test data (points [2, 39, 41-43]) for (a) the area fraction of precipitates, (b) and (c) the precipitate diameter.

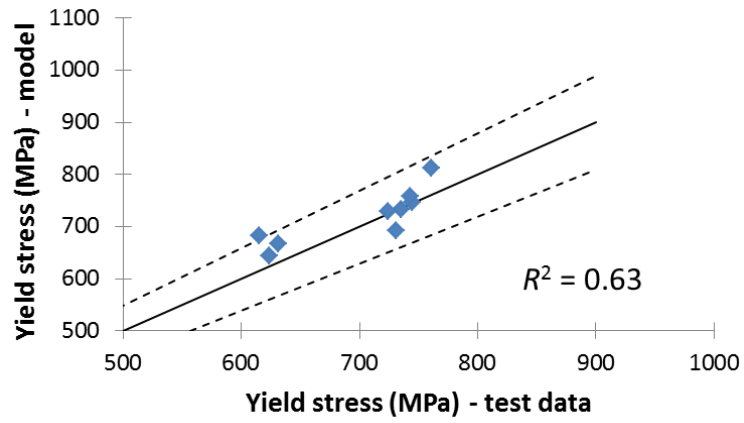
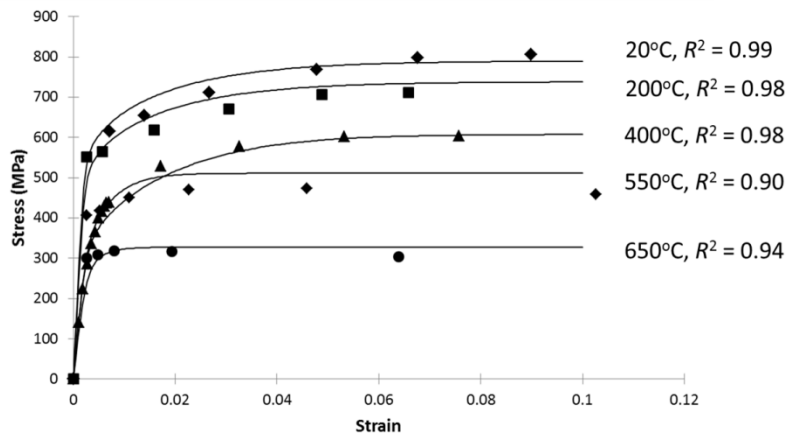
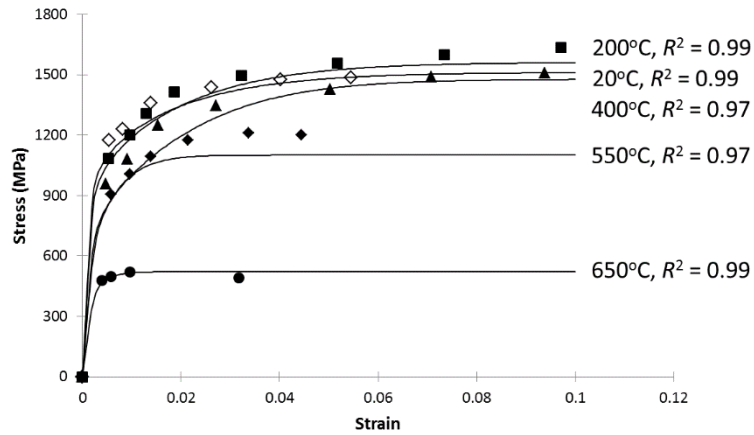


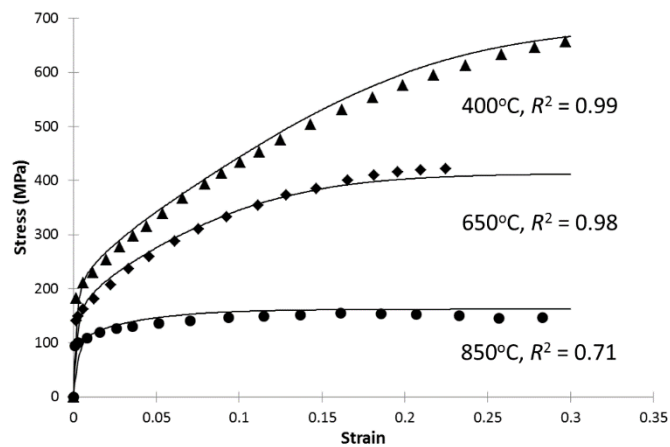
Fig. 8. A comparison between predicted yield stress and test data [39] at room-temperature. The dotted lines represent deviations of 10% from a perfect match.



(a)



(b)



(c)

Fig. 9. Calibration of the material model (lines) against test data [31] (points) for (a) tempered martensite, (b) newly-formed martensite and (c) austenite P92 across a range of temperatures.

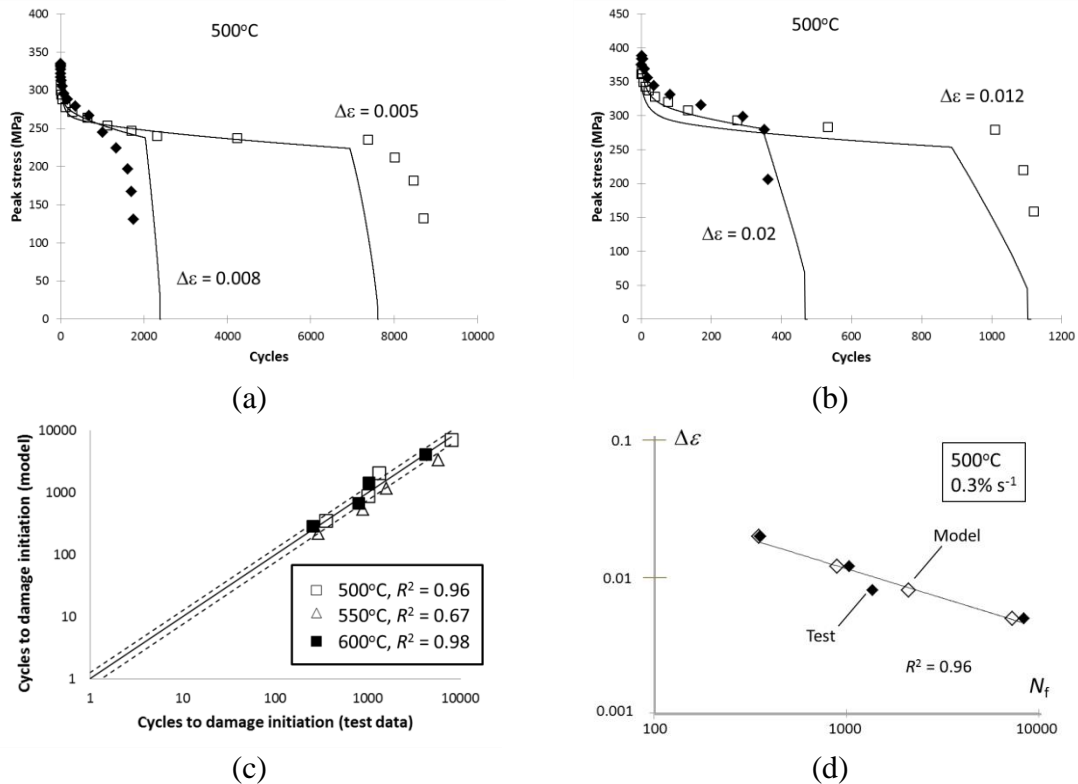


Fig. 10. Calibration of the cyclic-softening model against test data [47] at 500°C at strain-ranges of (a) 0.5% and 0.8% and (b) 1.2% and 2%, at a constant strain-rate ($0.3\% \text{ s}^{-1}$); comparisons between the experimentally-observed [47] and modelled number of cycles to damage initiation (taken as sudden drop in peak-stress) for (c) strain-ranges of 0.5%, 0.8%, 1.2% and 2% at different temperatures at a strain-rate of 0.3% (the dotted lines represent deviations of 25% from a perfect match) and (d) sample strain-life results for 500°C.

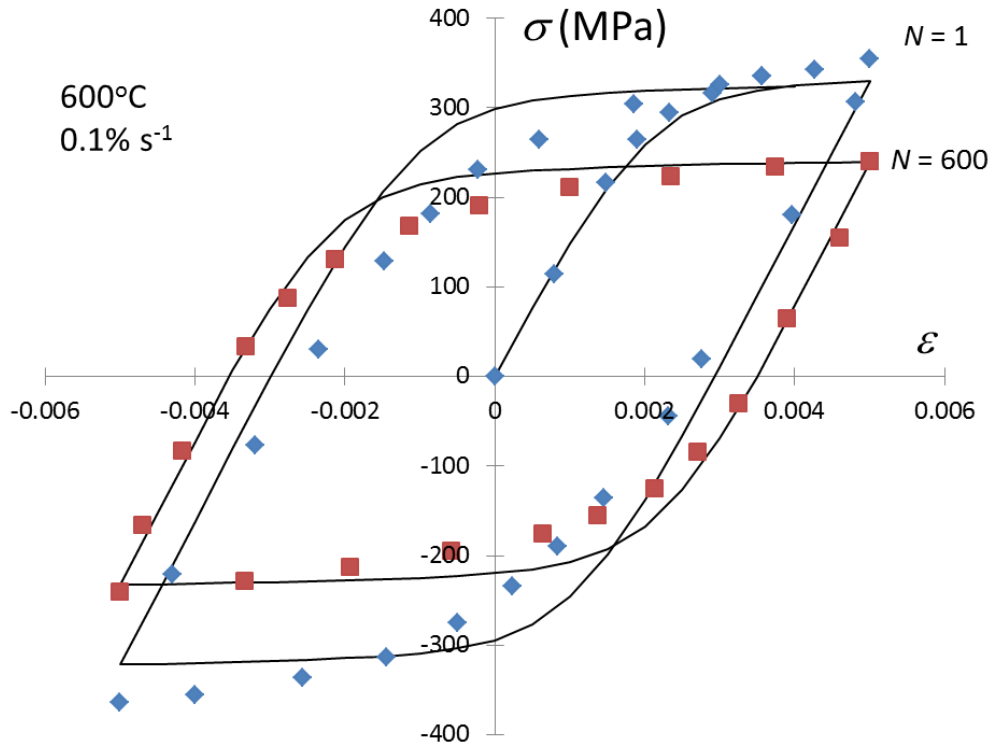


Fig. 11. A comparison between cyclic data for P91 PM [48] (points) and the current model for the first and 600th cycle at 600°C, strain-rate 0.1%/s and strain-range 1%.

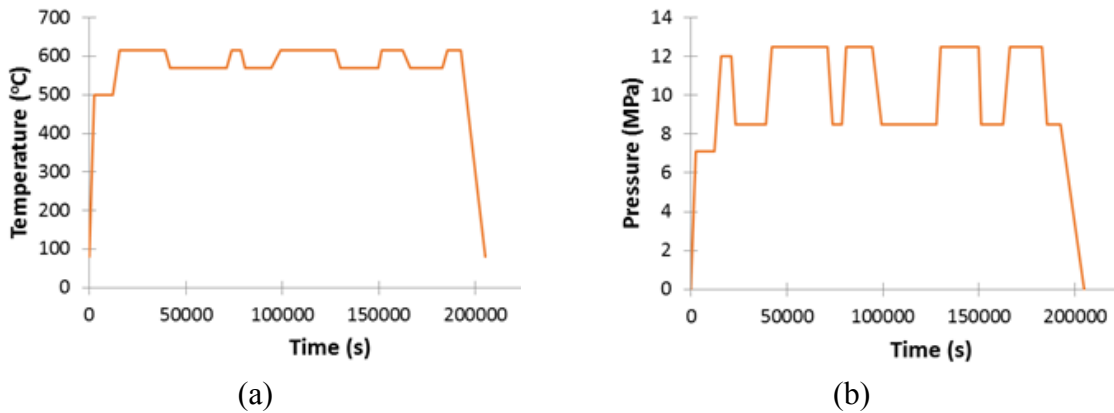


Fig. 12. The (a) temperature-time and (b) pressure-time histories to which the FE geometry is subjected following welding and PWHT.

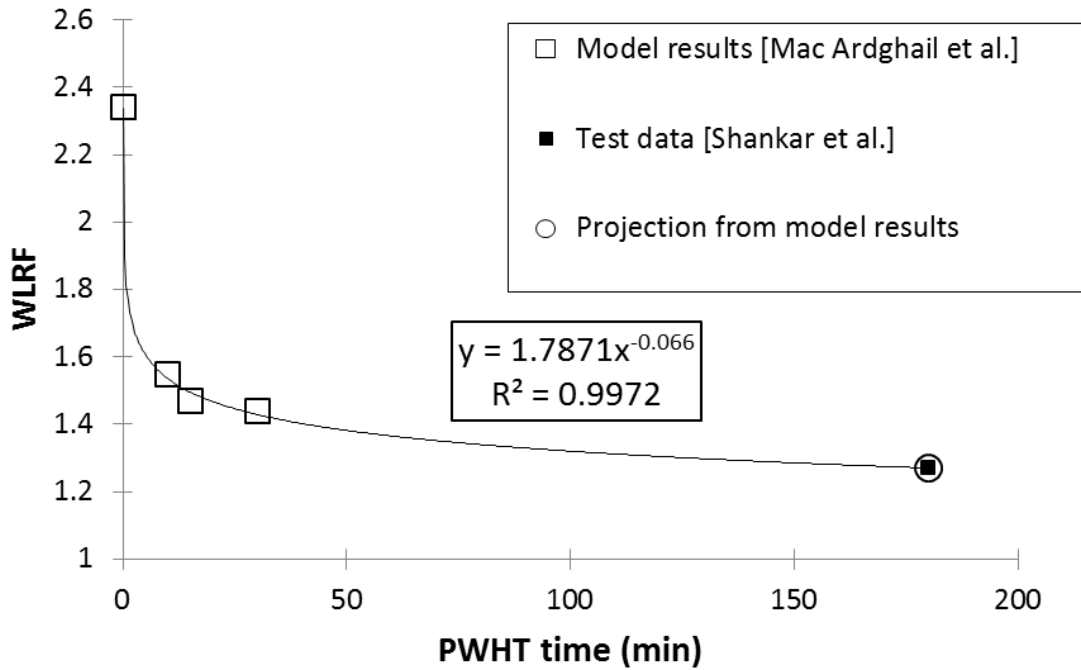


Fig. 13. Extrapolation of through-process prediction [27] of WLRf from short-term PWHT times to long-term PWHT times for comparison against long-term PWHT test data with a trend-line projection to experimental WLRf for P91 at 600°C, strain-range 2%, strain-rate 0.3% [6].

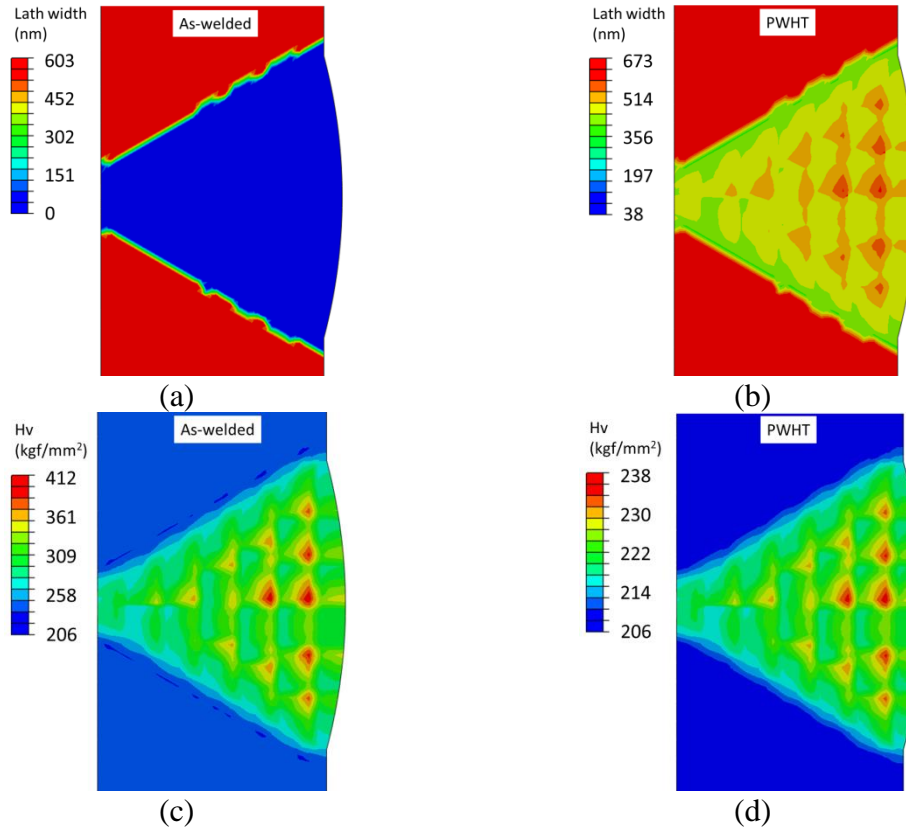


Fig. 14. The predicted lath-width [(a) and (b)], Vickers hardness [(c) and (d)], carbide diameter [(e) and (f)] and carbide area fraction [(g) and (h)] results for Case A in the as-welded and PWHT conditions.

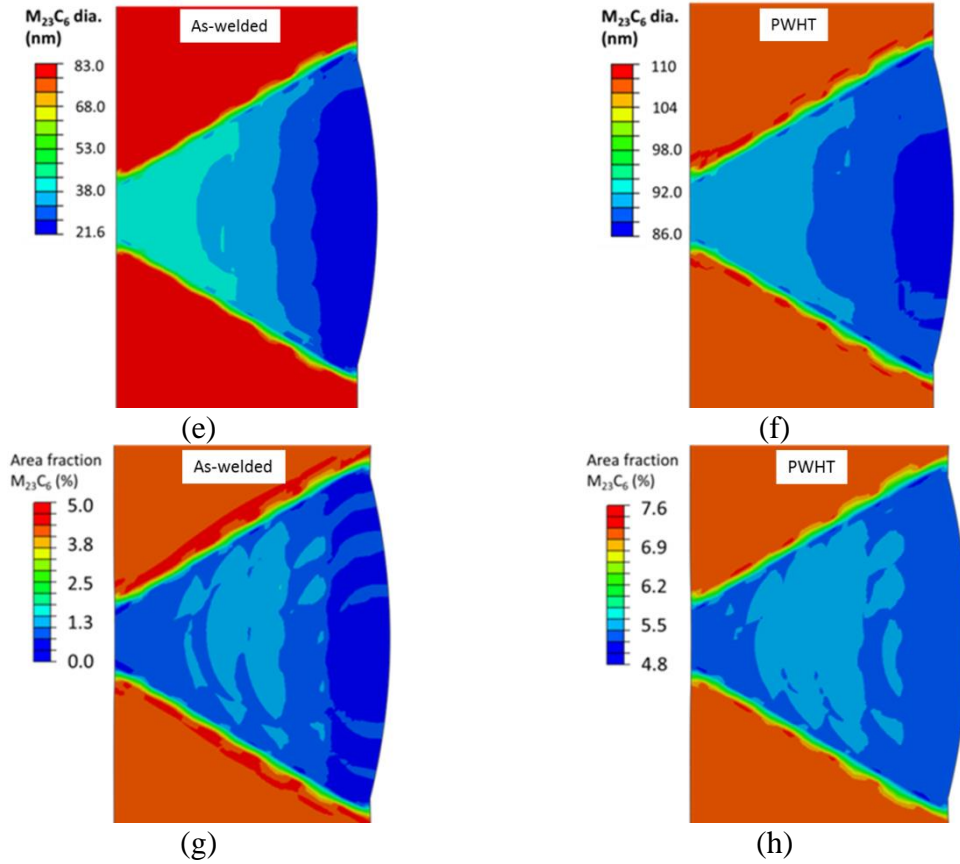


Fig. 14 (cont'd). The predicted lath-width [(a) and (b)], Vickers hardness [(c) and (d)], carbide diameter [(e) and (f)] and carbide area fraction [(g) and (h)] results for Case A in the as-welded and PWHT conditions.

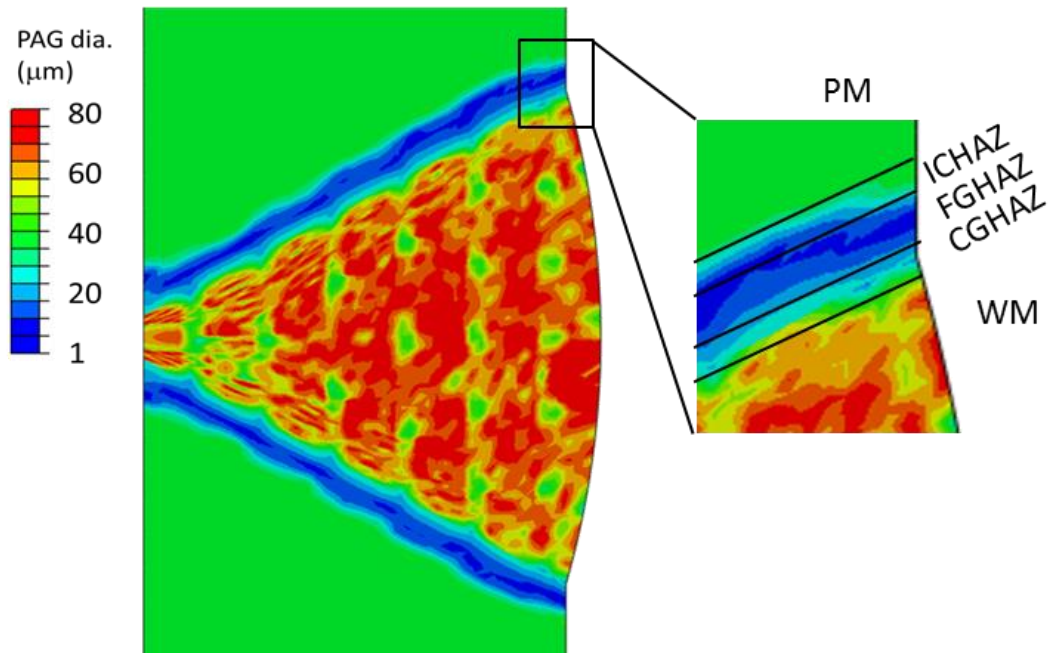


Fig. 15. The predicted prior-austenite grain size results for Case A for both the as-welded and PWHT conditions, showing separate predicted HAZ regions.

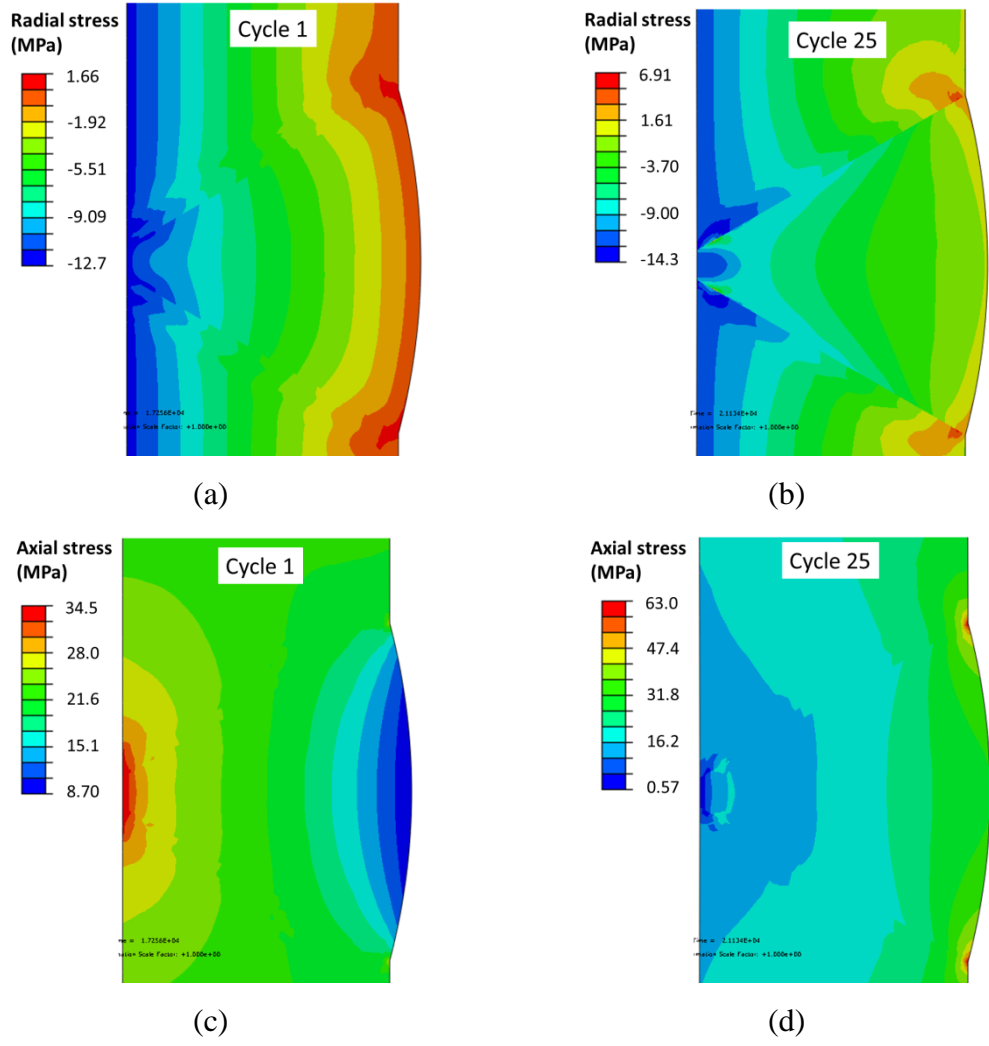


Fig. 16. Predicted stress contour plots for radial (a, b), axial (c, d) and hoop (e, f) for the first dwell period in the 57-hour in-service cycle for the first and 25th in-service cycles and the precipitate diameter distribution for the 25th cycle (g) for Case A.

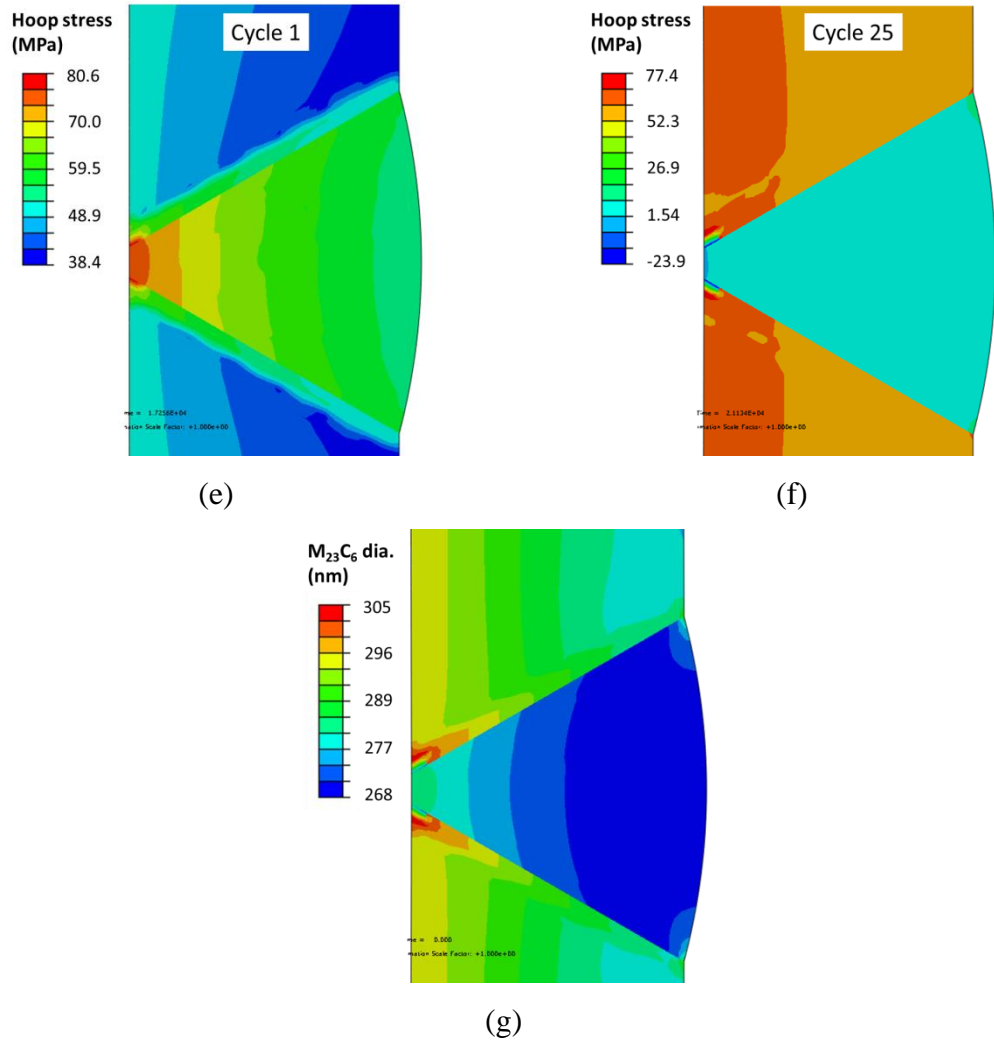


Fig. 16 (cont'd). Predicted stress contour plots for radial (a, b), axial (c, d) and hoop (e, f) for the first dwell period in the 57-hour in-service cycle for the first and 25th in-service cycles and the precipitate diameter distribution for the 25th cycle (g) for Case A.

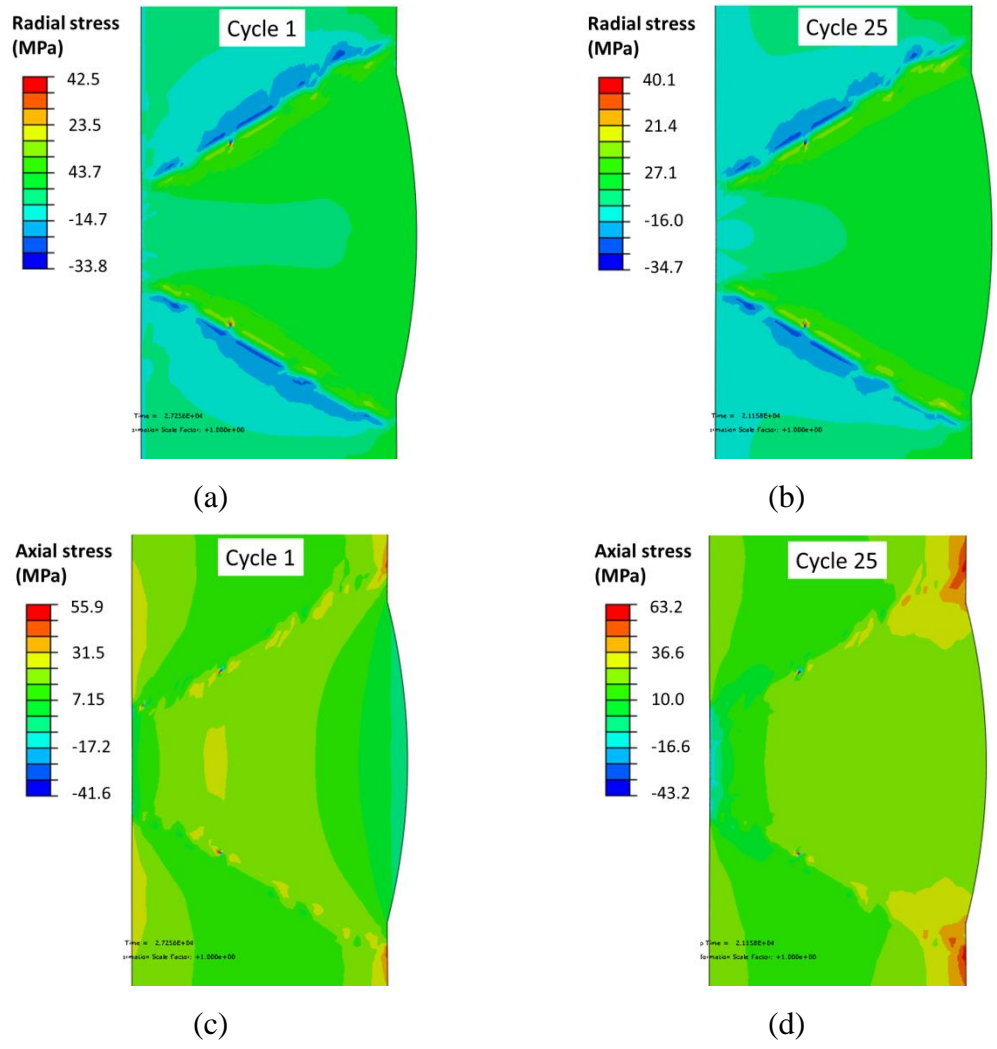
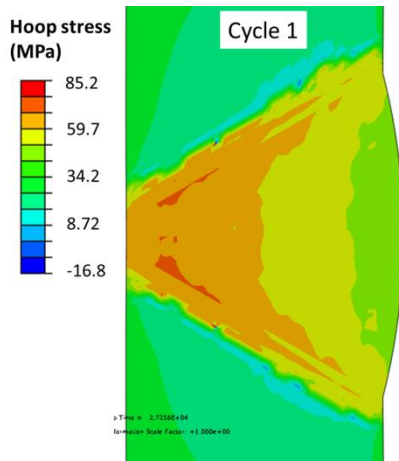
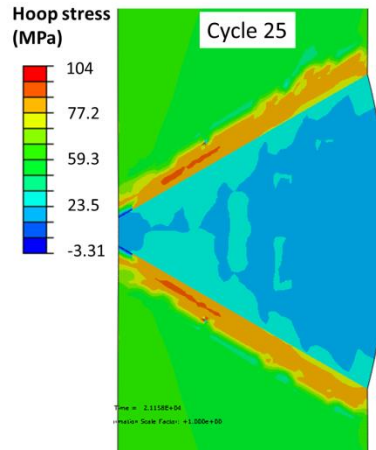


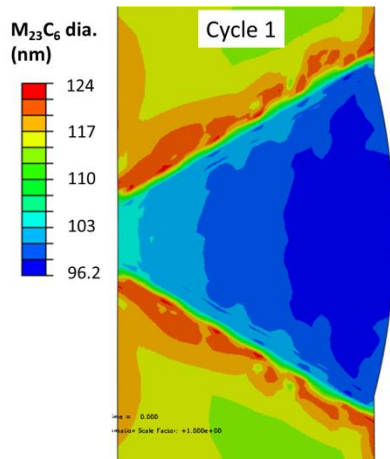
Fig. 17. Predicted stress contour plots for radial (a, b), axial (c, d) and hoop (e, f) for the first dwell period in the 57-hour in-service cycle for the first and 25th in-service cycles and the precipitate diameter distribution for the first and 25th cycle for Case D.



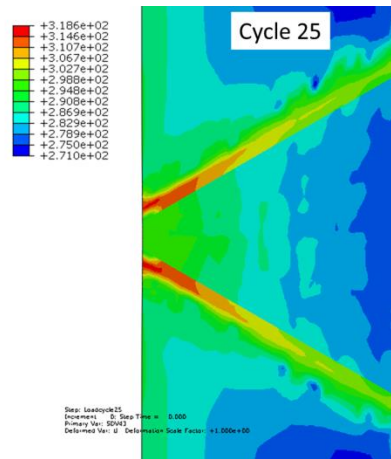
(e)



(f)



(g)



(h)

Fig. 17 (cont'd). Predicted stress contour plots for radial (a, b), axial (c, d) and hoop (e, f) for the first dwell period in the 57-hour in-service cycle for the first and 25th in-service cycles and the precipitate diameter distribution for the first and 25th cycle for Case D.

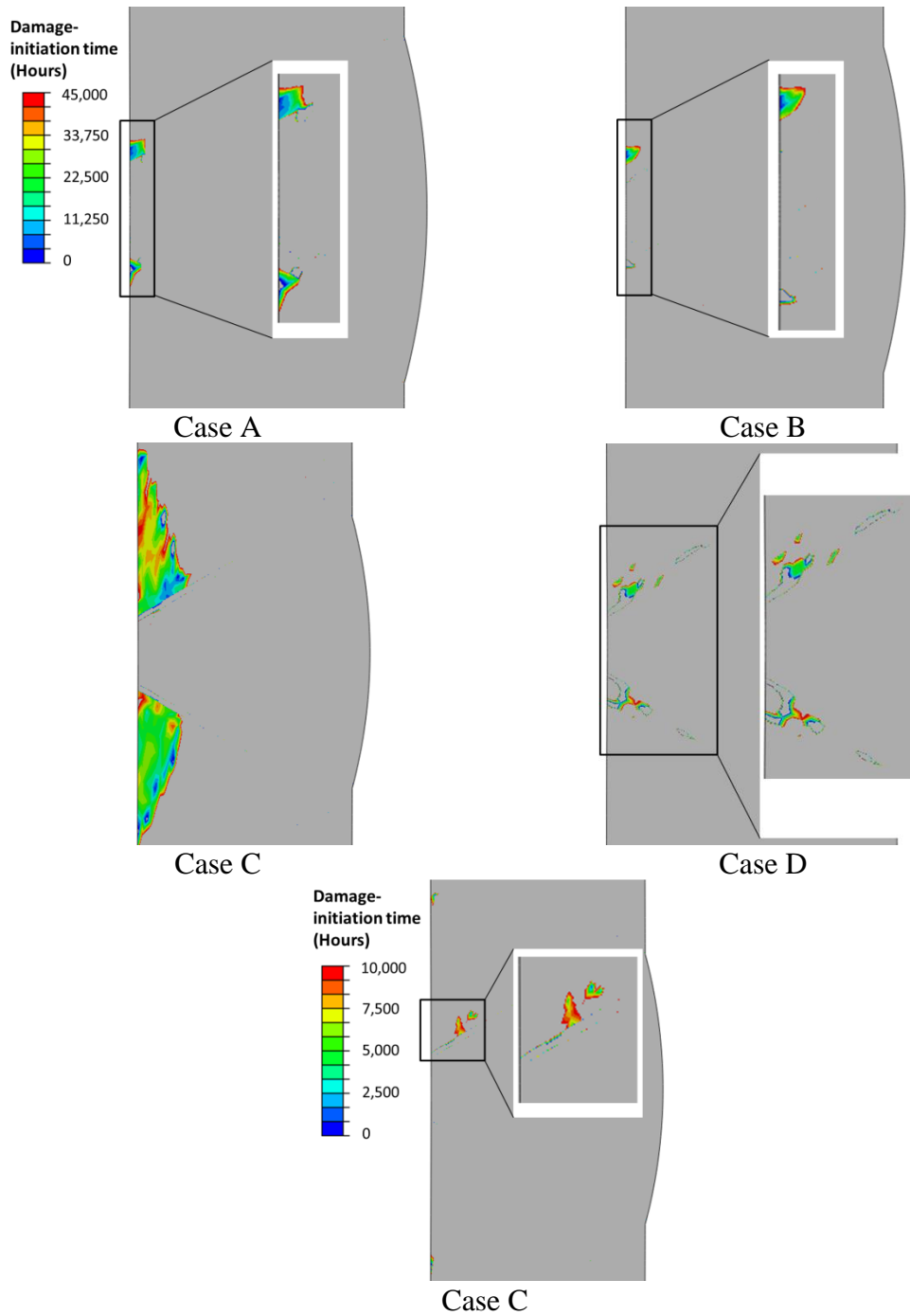


Fig. 18. Contour plots of predicted damage initiation times under 45,000 hours for Cases A to D and the contour plot of predicted damage initiation times under 10,000 hours for Case C.

Appendix A: Double-sigmoid equations

In this work, the parameters g_1 and $\bar{\rho}_L$ for martensite are defined by double-sigmoid equations as follows:

$$g_1 = 0.5(J_p + J_s) + \frac{J_{r1}(T - J_{T1})0.5(J_p - J_s)}{\sqrt{1 + (J_{r1}(T - J_{T1}))^2}} + \frac{J_{r2}(T - J_{T2})0.5(J_f - J_p)}{\sqrt{1 + (J_{r2}(T - J_{T2}))^2}} + 0.5(J_f + J_p) \quad (\text{A.1})$$

$$\bar{\rho}_L = 0.5(P_p + P_s) + \frac{P_{r1}(T - P_{T1})0.5(P_p - P_s)}{\sqrt{1 + (P_{r1}(T - P_{T1}))^2}} + \frac{P_{r2}(T - P_{T2})0.5(P_f - P_p)}{\sqrt{1 + (P_{r2}(T - P_{T2}))^2}} + 0.5(P_f + P_p) \quad (\text{A.2})$$

The seven parameters controlling the rate-term, g_1 , are constants (Table A.1). It was found that the parameters P_p, P_s, P_f, P_{r1} and P_{r2} are dependent on the lath width whereas P_{T1} and P_{T2} are not (Table A.1).

In the austenite phase, g_1 (Eqn. 23) is defined by a linear equation:

$$g_1 = g_2 + g_3T \quad (\text{A.3})$$

and $\bar{\rho}_L$ (austenite phase) is defined by:

$$\bar{\rho}_L = 0.5(P_p^\gamma + P_s^\gamma) + \frac{P_{r1}^\gamma(T - P_{T1}^\gamma)0.5(P_p^\gamma - P_s^\gamma)}{\sqrt{1 + (P_{r1}^\gamma(T - P_{T1}^\gamma))^2}} \quad (\text{A.4})$$

The model parameters for Eqns. A.3 and A.4 are shown in Table A.1.

Table A.1. Identified parameters for the dislocation-density evolution model

Parameter	Value
J_p	383
J_s	55
J_f	90
J_{r1}	0.015 K ⁻¹
J_{r2}	0.05 K ⁻¹
J_{T1}	550 °C
J_{T2}	720 °C
P_p	$0.867 - 0.014(\text{nm}^{-0.5})\sqrt{L}$
P_s	$0.27 - 0.0024(\text{nm}^{-0.5})\sqrt{L}$
P_f	$0.0976 - 0.0009(\text{nm}^{-0.5})\sqrt{L}$
P_{r1}	$-0.0077 + 0.0015(\text{nm}^{-0.5})\sqrt{L}$
P_{r2}	$0.0225 + 0.0003(\text{nm}^{-0.5})\sqrt{L}$
P_{T1}	275 °C
P_{T2}	555 °C
g_2	6.443
g_3	0.0225 K ⁻¹
P_p^γ	0.3
P_s^γ	0.9
P_{r1}^γ	0.01 K ⁻¹
P_{T1}^γ	710 °C